ISSN 2718-322X (Online)

Engineering Power

BULLETIN OF THE CROATIAN ACADEMY OF ENGINEERING Vol. 21(2) 2026



EDITOR-IN-CHIEF'S WORD

Dear readers,

Artificial intelligence is rapidly transforming engineering, not only by providing new computational tools but also by changing the way we approach scientific and technological challenges. Its true potential lies in combining data-driven methods with established scientific knowledge, engineering expertise, and a sound understanding of physical principles.

The Croatian Academy of Engineering is committed to promoting scientific excellence, encouraging interdisciplinary cooperation, and fostering the responsible application of emerging technologies. Through Engineering Power, we aim to contribute to the exchange of knowledge and ideas that advance both engineering research and professional practice.

This issue also marks an important moment in the Academy's institutional life, as its 59th Annual General Assembly provided an opportunity to reflect on past achievements, recognize outstanding contributions, and welcome new leadership for the years ahead.

I trust that this issue will provide valuable insights and inspire further research and collaboration.

Editor-in-Chief
Vedran Mornar, President of the Croatian Academy of Engineering



EDITOR'S WORD

Dear readers,

It is a particular pleasure to present new issue of Engineering Power, edited by Marko Čanađija and Lovre Krstulović-Opara, members of the Croatian Academy of Engineering from the Department of Mechanical Engineering and Naval Architecture. This issue contains three papers that demonstrate the integration of artificial intelligence and machine learning with classical methods in experimental and computational mechanics. In addition to these papers, this issue also includes a review of the 59th Annual General Assembly of the Croatian Academy of Engineering, held on June 8, 2026 in Zagreb.

I hope you enjoy reading this issue.

Editor
Bruno Zelić, Vice-President of the Croatian Academy of Engineering





FOREWORD

Artificial intelligence (AI) and machine learning (ML) are becoming increasingly important tools in modern engineering, opening new possibilities for the analysis, modelling, and optimisation of mechanical systems and materials. Their integration with established numerical and experimental methods offers opportunities to address complex problems that are difficult or computationally demanding to solve using conventional approaches alone.

This special issue of Engineering Power, entitled Applications of Artificial Intelligence and Machine Learning in Experimental and Computational Mechanics, presents three contributions that illustrate different aspects of this rapidly developing field. The first paper, by Čanađija, Ivić, and Zlatić, presents a computational framework for the optimal design of metamaterials based on carbon-nanotube nanotrusses. Molecular dynamics simulations are first used to generate a dataset describing the stress–strain behavior of single-walled carbon nanotubes. A neural network augmented with fundamental physical constraints is then trained on this dataset and subsequently employed as a surrogate constitutive model in nonlinear finite element analyses. This approach preserves the high accuracy of molecular dynamics simulations while significantly reducing the associated computational cost. In the final step, the framework is integrated with optimization algorithm, resulting in an efficient computational tool for developing metamaterials with tailored mechanical properties.

The second contribution, by Zlatić and Čanađija, addresses the incorporation of physical constraints into neural-network-based constitutive models for hyperelastic materials undergoing finite deformations. These types of constitutive models are more convenient than conventional models because they do not require a predefined functional form. The paper provides details on the proper enforcement of thermodynamic consistency, objectivity, energy normalisation, and polyconvexity. The resulting neural-network model is then implemented in the finite element software Abaqus as a replacement for a conventional constitutive model. The presented example demonstrates the performance of the proposed procedure in a hyperelastic application relevant to rubber and biological materials.

The third paper, by Grebo and Krstulović-Opara, explores the application of deep learning to experimental mechanics by investigating the relationship between full-field measurements obtained using Digital Image Correlation (DIC) and Infrared Thermography (IRT). Using a U-Net architecture, the authors compare the prediction of thermal fields from measured strain distributions with the reverse mapping from temperature to strain fields. The results highlight both the potential and limitations of neural networks for integrating complementary experimental measurement techniques.

Although addressing different problems, the three contributions share a common objective: combining the capabilities of AI and ML with established physical principles, numerical methods, and experimental observations. They demonstrate that data-driven approaches are particularly valuable when used to complement, rather than replace, conventional methods in mechanics.

Guest Editors
Marko Čanađija, University of Rijeka, Faculty of Engineering
Lovre Krstulović-Opara, University of Split, Faculty of Electrical Engineering, Mechanical Engineering and Naval Architecture

CONTENT

Editors' Words 1
1. Tailored metamaterials based on carbon nanotube nanotrusses: A molecular dynamics–neural network–finite element framework 2
2. On the implementation of physical constraints for neural network modeling of hyperelastic materials at finite strains 7
2. Comparison of U-Net-based mapping from DIC-derived effective strain to infrared thermography data and from infrared thermography data to DIC-derived effective strain 12
3. 59th Annual General Assembly of the Croatian Academy of Engineering 24

Marko Čanađija[1,], Stefan Ivić[1], Martin Zlatić[1]*

Tailored metamaterials based on carbon nanotube nanotrusses: A molecular dynamics–neural network–finite element framework

[1]Faculty of Engineering, University of Rijeka, Vukovarska 58, 51000 Rijeka, Croatia
*Corresponding author: marko.canadija@riteh.uniri.hr

Original scientific paper
Received: July 17, 2025
Accepted: March 6, 2026
https://doi.org/10.65776/ep.21.2.1

This work is licensed under a Creative Commons Attribution 3.0 Unported License.

Abstract

The paper at hand deals with the optimal design of metamaterials. As a fundamental building block of such metamaterials, a nanotruss is used, preserving the benefits of classical macroscopic trusses. Each truss element is made of a single-walled carbon nanotube. Such a choice should ensure superior strength of this class of metamaterials. Due to the repetitive nature of the optimization process, a computationally efficient framework is required. On the other hand, molecular dynamics is considered to be the most accurate, albeit prohibitively slow for this purpose. To achieve this goal, machine learning is used. More specifically, a partially input convex neural network takes the role of a constitutive model for all single-walled carbon nanotube configurations of practical interest. This network also incorporates fundamental principles of physics. Convexity is included in the architecture of the neural network and addresses the issue of noise caused by temperature effects. It is important to emphasize that the neural network is trained on a dataset obtained by molecular dynamics, and thus retains the accuracy of molecular dynamics. The developed neural network is then coupled to the Abaqus finite element code, providing constitutive behavior to nonlinear finite element calculations. Finally, the framework is linked to the optimization code Indago. The performance of the framework is demonstrated on an example. It is concluded that the framework is computationally efficient, yet accurate. The strong nonlinear apparatus available in Abaqus ensures the versatility of the framework.

***Keywords**: single-walled carbon nanotubes; partially input convex neural networks; shape optimization; metamaterials; molecular dynamics.*

1. Introduction

Nowadays, the focus of many researchers is oriented toward the development of metamaterials with extreme material properties. The building blocks of such metamaterials usually are hierarchical nanotruss structures [1], made either of polymers or ceramics [1], or of carbon [2]. Using a truss structure as a building block ensures the well-known macroscopic engineering properties of trusses - used for thousands of years - as lightweight structures with high load capacity. The most intriguing property of such metamaterials is that they possess the strength of conventional steel, while having a specific mass density comparable to that of Styrofoam.

The present research considers single-walled carbon nanotubes (SWCNTs) as the truss elements. Although such structures have not yet been fabricated in laboratories, this academic study nevertheless aims to develop a computational framework that could be used to investigate them. The choice of SWCNTs is justified by molecular dynamics (MD) simulations of uniaxial tensile loading, which demonstrate that they possess theoretical ultimate tensile strengths up to 200 times greater than that of conventional structural steels [3]. Although the presence of defects - such as atomic vacancies, topological irregularities, and interfacial discontinuities - can significantly reduce their effective strength, SWCNTs still retain exceptional mechanical properties. This makes them promising candidates for reinforcing composite materials where both strength and weight savings are important. These nanocomposites are already finding application in lightweight, high-performance sporting equipment, as well as in the aerospace, automotive, and defense sectors.

Beyond the conventional use of single-walled carbon nanotubes (SWCNTs) as reinforcement in composite materials, as already indicated, this research aims to analyze

SWCNTs as fundamental components of nanotruss structures. However, a major bottleneck in the development and analysis of such SWCNT-based truss materials is the lack of an adequate computational framework. Several modeling strategies are available, but each has significant limitations:

- Molecular Dynamics (MD): MD simulations are often considered the most realistic due to the inclusion of atomic interactions and thermal effects. The methodology is now well-established for simulating mechanical problems at the nanoscale. Unfortunately, the computational cost of MD becomes prohibitive when applied to structures involving large numbers of atoms, such as those found in SWCNT-based trusses. This effectively rules out repetitive calculations, such as those required in optimization.
- Finite Element Method (FEM): FEM is often a straightforward choice and, in this context, is known as Molecular Structural Mechanics (MSM) [4, 5]. MSM models the carbon–carbon bonds in SWCNTs as beam finite elements with equivalent stiffnesses. The method is computationally efficient but is often restricted to linear formulations and offers significantly reduced accuracy compared to MD, even when nonlinearities are partially included. Furthermore, the method leads to a large number of elements, since each C-C bond must be explicitly modeled.
- Analytical Nonlocal Elasticity Models: Nonlocal continuum models attempt to capture nanoscale effects by introducing an additional length-scale (small-size) parameter [6]. This parameter extends the classical constitutive equations to account for atomic-scale interactions, i.e., small-size effects. This approach leads to mathematically sound beam models; however, it depends heavily on the precise value of the nonlocal parameter. This parameter is not easily determined—it can be obtained from MD or experimental data, but its small magnitude makes it highly sensitive to noise introduced by thermal vibrations in MD simulations or to measurement limitations in experimental setups. For this reason, most MD simulations are performed at 0 K. This remains a serious issue in the application to real engineering structures.

Thus, it is clear that all existing approaches suffer from serious drawbacks. For this reason, the present research proposes a fourth modeling strategy that combines the atomistic accuracy of MD with the efficiency of FEM. Each SWCNT is modeled as a single rod-like finite element, rather than using individual beam finite elements to represent atomic bonds. The small-size parameter will be included implicitly in the formulation, eliminating the need to incorporate it as a separate parameter explicitly. This is achieved by substituting the classical constitutive model with a neural network (NN). The NN will be trained on a large dataset obtained from MD simulations of uniaxial tension and compression of individual SWCNTs. This paper presents only the central ideas of the framework, while further details and examples can be found elsewhere [1, 8–10].

2. Molecular Dynamics – Uniaxial Tension and Compression Test of SWCNTs

In order for the NN to achieve the same reliability as MD, it is clear that it should be trained on data produced by MD. To this end, a comprehensive set of 818 different SWCNTs, including all possible configurations up to 4 nm in diameter, was prepared. The length-to-diameter ratio was approximately 5 in all cases. The SWCNT lengths ranged from 1.899 to 19.836 nm, while the smallest and largest configurations were (4,1) and (50,2) nanotubes, respectively. Tension and compression MD simulations were carried out using LAMMPS [11] at a temperature of 300 K. Note that introducing a temperature higher than 0 K causes stochastic vibrations of atoms, which in turn induce vibrations in the entire nanotube structure. Such vibrations can be regarded as unwanted noise inherently present in the results. To alleviate issues caused by stochastic vibrations associated with temperature, each test was performed three times, and the results were averaged. The main results were true stress - true strain curves for each SWCNT, evaluated under both tension and compression.

The governing potential was the modified AIREBO [12], which is often considered the most accurate among classical potentials. One end of each SWCNT was held fixed, while a velocity was prescribed at the other end such that the strain rate was 0.001 ps^{-1} for every SWCNT configuration considered. For further details, see [3, 8–10]. The equilibration time was 25 ps, and the time step was 0.5 fs.

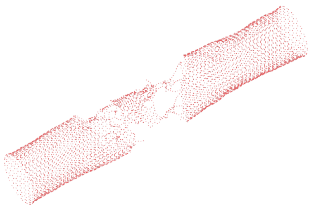


Fig. 1. Tensile fracture of (20,20) SWCNT

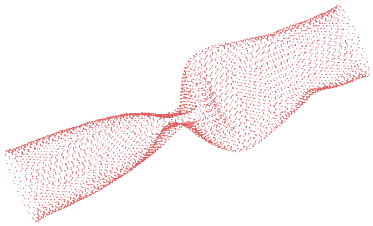


Fig. 2. Shell-like buckling of (20,20) SWCNT

3. Neural Networks and Convexity

The dataset obtained from MD simulations consisted of points, where each point was defined by the following data: true stress, true strain, and the chirality parameters n and m for the particular SWCNT. The complete dataset consisted of approximately three million points, or 3700 in average.

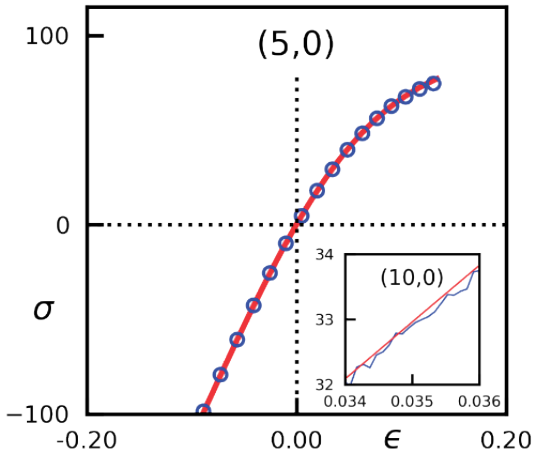


Fig. 3. True stress–true strain curve for a (5,0) SWCNT. The inset shows a detail of the stress–strain curve for a (10,0) SWCNT. The red curve represents results obtained by the NN, while the blue curve corresponds to the MD results. Stresses are given in GPa.

With this dataset at hand, a neural network was trained. Initial attempts [8], carried out with three different types of NNs, showed that all were able to capture stress-strain curves with remarkable accuracy. In particular, all noise induced by the stochastic vibrations related to temperature (blue line in the inset of Fig. 3) was reproduced by the NN. It is clear that the stresses do not monotonically increase with strain. This, in turn, leads to negative tangent moduli, which effectively rules out the application of such NNs in nonlinear finite element calculations due to convergence issues.

An additional problem stemming from the violation of monotonicity is the loss of convexity of the strain energy with respect to strain. Although the convexity requirement is often considered too strict [13, 14], it is necessary in the present one-dimensional case involving truss elements. For this reason, the neural network should be designed to ensure that the strain energy is convex with respect to strain. However, since the chirality parameters n and m are also inputs to the NN, convexity constraints should not be imposed on these parameters.

Feed-forward neural networks of this kind are known as partially input convex neural networks (PICINNs) and were first described by Amos et al. [15] in 2017. The same authors also introduced neural networks whose output is convex with respect to the entire input. The latter type of networks is now frequently used in computational mechanics [16–18], while PICINNs are less common [19]. The cornerstone of such networks relies on well-known theorems from convexity theory. In particular, a function is convex if it is a composition of non-decreasing convex functions and if it is a sum of non-negative convex functions. If an additional requirement is integrability, this leaves the Softplus activation function as the only choice. To summarize, a neural network designed in this manner is convex with respect to its input by design. Further modifications can make this network partially input convex [15, 9].

Additionally, it is advantageous to include other physics-based conditions in the design of the network. In particular, the PICINN described above requires that the strain energy be a convex function of strain. This implies that NN training should be performed using strain–energy pairs. Although the energy could be estimated from the available stress–strain data, this procedure would be cumbersome. To address this issue, the network is designed with strain (and chirality parameters) as inputs, and strain energy as the output. However, autodifferentiation capabilities are exploited so that training is performed on stress–strain pairs, a method known as Sobolev training. This means that stress is the first derivative of strain energy with respect to strain, automatically ensuring thermodynamic consistency. The approach also exactly satisfies the requirements that energy and stress vanish at zero strain. Finally, the growth condition (energy tending to infinity as strain tends to infinity) and the condition that energy is non-negative are also fulfilled. In the present case, the PICINN is developed using TensorFlow 2.

The trained PICINN can then serve as the constitutive model, providing strain energy and stresses for a given strain. Further differentiation also yields the tangent modulus. The final step is coupling the model to the UMAT subroutine in Abaqus, resulting in a very general framework suitable for solving a variety of nonlinear problems involving trusses. Such a procedure could not be performed with MD due to the exceptional computational costs involved. For comparison, a single SWCNT tensile test MD simulation lasted from 6 minutes for the smallest SWCNT to 6 hours for the largest one. Using the trained PICINN as a surrogate reduced this time to a fraction of a second. Thus, the present approach differs from the classical MSM approach. In the classical MSM approach, each rod (or, more commonly, beam) represents the forces between atoms. In contrast, in the present approach each rod represents an entire nanotube rather than the interaction between individual atoms. By adjusting the rod material properties using PICINN, an accurate yet computationally inexpensive method is obtained.

4. Optimization Framework

In the MD-NN-FEM framework presented here, the computational costs are reduced significantly. This, in turn, enables repetitive procedures like optimization to be carried out within a realistic timeframe. While the MD – NN - FEM framework provides a computational tool for simulating carbon nanotube - based nanotrusses, tailored properties of some metamaterials can be achieved through optimization. This can include reducing the weight of a nanostructure, maximizing the stored elastic energy in a metamaterial, minimizing the Poisson's ratio to obtain an auxetic material, or increasing the compressive strength. Other possibilities also exist.

The optimization tool used for the present study is Indago [20]. The optimization performed can be classified as shape optimization. In particular, several variables defining the geometry of the nanotruss are selected, and a mesh suitable for the Abaqus FEA code is produced. The methods used in this research were Nelder–Mead (NM)

[21], Particle Swarm Optimization (PSO) [22], Artificial Bee Colony optimization (ABC) [23], Squirrel Search Algorithm (SSA) [24], and Bat Algorithm (BA) [25]. The best global minimum was always obtained by the Nelder–Mead method, albeit at the cost of a higher number of optimization repetitions. PSO and SSA also demonstrated very good performance, while ABC and BA showed inferior results.

5. Example

As an illustration of the framework's performance, an energy-trapping metamaterial is considered. The nanotruss based on SWCNTs is motivated by the research in [26], where bi-stable structures were studied. While in [26] beams connecting two rigid layers buckle elastically and can assume a second stable configuration, in the present case, a nanotruss replaces the beam (Fig. 4). Note that the stored energy can be recovered by reversing the direction of the load.

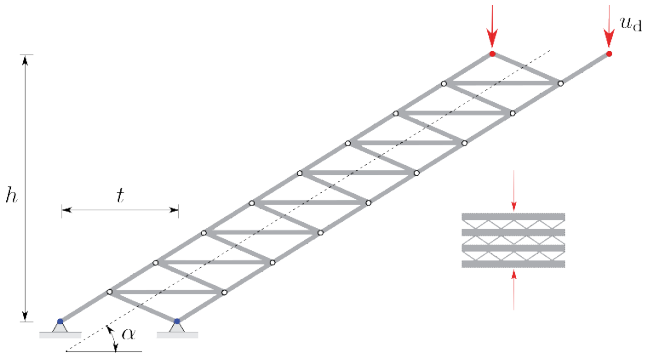


Fig. 4. Basic building element of an energy trapping metamaterial, along with the variables used in optimization.

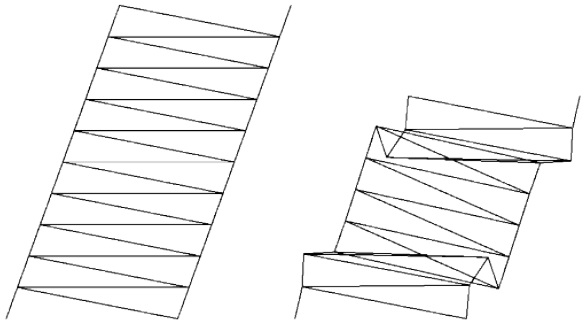


Fig. 5. Initial and final configuration of an energy trapping nanotruss.

Shape optimization was performed to find the variables t, h and α that produce a structure capable of storing as much energy as possible. Constraints were imposed on the allowable stresses, as well as on the maximum length of each SWCNT, which was limited to no more than 12.5 times its diameter. This latter constraint ensured that beam-like buckling of each nanotube could not occur. The nanotruss was made of (7,0) SWCNTs.

Global optimum was obtained for t=4.534 nm, h=8.257 nm, α=70.048° while stored energy was 37.98 nN nm, Fig. 5. The final configuration shows that a rigid rotation of the central part of the nanotruss occurs, effectively locking the stored energy.

For more details, see [10].

6. Concluding Remarks

The research presented a tool that maintains simulation costs at the level of finite element analysis while preserving the accuracy of molecular dynamics. This outcome was achieved through the application of feed-forward neural networks that serve as the constitutive model.

However, straightforward use of a standard feed-forward neural network is not possible; instead, one must rely on the PICINN extension, incorporating fundamental physics constraints directly into the NN architecture. The PICINN was coupled to the standard FEM code Abaqus, thereby ensuring both the generality of the approach and the availability of Abaqus's robust numerical capabilities.

Finally, the MD-NN-FEM procedure was coupled to the optimization code to enable the design of metamaterials with tailored properties.

The example demonstrated the applicability and efficiency of the developed framework. This versatile framework can be applied to any problem involving the optimal design of carbon nanotube–based nanotrusses.

Acknowledgements

This work has been supported in part by the Croatian Science Foundation under the project IP-2019-04-4703 and in part by the University of Rijeka, Croatia under project numbers: uniri-iskusni-tehnic-23-37 and uniri-mzi-25-16. This support is gratefully acknowledged.

7. References

[1] Meza, L.R., Zelhofer, A.J., Clarke, N., Mateos, A.J., Kochmann, D.M., Greer, J.R. Resilient 3D hierarchical architected metamaterials. Proc. Nat. Acad. Sci. 112 (2015) 11502-11507.

[2] Serles, P., Yeo, J., Haché, M., Demingos, P.G., Kong, J., Kiefer, P., Dhulipala, S., Kumral, B., Jia, K., Yang, S., Feng, T. Ultrahigh Specific Strength by Bayesian Optimization of Carbon Nanolattice. Adv. Mat. 37 (2025) 2410651.

[3] Čanađija, M. Deep learning framework for carbon nanotubes: Mechanical properties and modeling strategies. Carbon 184 (2021) 891-901.

[4] Li, C., Chou, T.W. A structural mechanics approach for the analysis of carbon nanotubes. Int. J. Solids Struct. 40 (2003) 2487-2499.

[5] Barretta, R., Brčić, M., Čanađija, M., Luciano, R., de Sciarra, F.M. Application of gradient elasticity to armchair carbon nanotubes: Size effects and constitutive parameters assessment. Eur. J. Mech. A-Solid 65 (2017) 1-13.

[6] Romano, G., Barretta, R., Diaco, M., de Sciarra, F.M. Constitutive boundary conditions and paradoxes in nonlocal elastic nanobeams. Int. J. Mech. Sci. 121 (2017) 151-156.

[7] Čanađija, M. Thermomechanics of Solids and Structures – Physical Mechanisms, Continuum Mechanics and Applications. Elsevier, Amsterdam, 2023.

[8] Košmerl, V., Štajduhar, I., Čanađija, M. Predicting stress–strain behavior of carbon nanotubes using neural networks. Neural Comput. Appl. 34 (2022) 17821-17836.

[9] Čanađija, M., Košmerl, V., Zlatić, M., Vrtovšnik, D., Munjas, N. A computational framework for nanotrusses: Input convex neural networks approach. Eur. J. Mech. A-Solid 103 (2024) 105195.

[10] Čanađija, M., Ivić, S. Carbon nanotubes as a basis of metamaterials and nanostructures: Crafting via design optimization. Mech. Mater. 197 (2024) 105105.

[11] Plimpton, S. Fast parallel algorithms for short-range molecular dynamics. J. Comp. Physics 117 (1995) 1-19.

[12] Shenderova, O.A., Brenner, D.W., Omeltchenko, A., Su, X., Yang, L.H. Atomistic modeling of the fracture of polycrystalline diamond. Phys. Rev. B: Condens. Matter, 61 (2000) 3877.

[13] Ball, J.M. Convexity conditions and existence theorems in nonlinear elasticity. Arch. Ration. Mech. Anal. 63 (1976) 337–403.

[14] Zlatić, M., Čanađija, M. Recovering Mullins damage hyperelastic behavior with physics augmented neural networks, J. Mech. Phys. Solids (2024) 105839.

[15] Amos, B., Xu, L., Kolter, J.Z. Input convex neural networks. In International conference on machine learning, July 2017, 146-155.

[16] As' ad, F., Avery, P., Farhat, C. A mechanics-informed artificial neural network approach in data-driven constitutive modeling, Int. J. Numer. Methods Eng., 123 (2022) 2738–2759.

[17] Klein, D.K., Fernández, M., Martin, R. J., Neff, P., Weeger, O.. Polyconvex anisotropic hyperelasticity with neural networks, J. Mech. Phys. Solids 159 (2022) 104703.

[18] Linden, L., Klein, D. K., Kalina, K. A., Brummund, J., Weeger, O., Kästner, M. Neural networks meet hyperelasticity: A guide to enforcing physics, J. Mech. Phys. Solids 179 (2023) 105363.

[19] Huang, S., He, Z., Reina, C. Variational Onsager Neural Networks (VONNs): A thermodynamics-based variational learning strategy for non-equilibrium PDEs. J. Mech. Phys. Solids, 163 (2022) 104856.

[20] Družeta, S., Ivić, S. Indago-Python module for numerical optimization (2020).

[21] Nelder, J.A., Mead, R. A simplex method for function minimization. Comput. J. 7 (1965) 308–313.

[22] Kennedy, J., Eberhart, R. Particle swarm optimization. In: Proceedings of ICNN'95-International Conference on Neural Networks. IEEE 4 (1995) 1942–1948.

[23] Karaboga, D., Akay, B. A comparative study of artificial bee colony algorithm. Appl. Math. Comput. 214 (2009) 108–132.

[24] Jain, M., Singh, V., Rani, A. A novel nature-inspired algorithm for optimization: Squirrel search algorithm. Swarm Evol. Comput. 44 (2019) 148–175.

[25] Yang, X.-S., Hossein Gandomi, A. Bat algorithm: a novel approach for global engineering optimization. Eng. Comput. 29 (2012) 464–483.

[26] Shan, S., Kang, S.H., Raney, J.R., Wang, P., Fang, L., Candido, F., Lewis, J.A., Bertoldi, K. Multistable architected materials for trapping elastic strain energy. Adv. Mater. 27 (2015) 4296-4301.

Zlatić Martin[1], Čanađija Marko[1,]*

On the implementation of physical constraints for neural network modeling of hyperelastic materials at finite strains

[1]Faculty of Engineering, University of Rijeka, Vukovarska 58, 51000 Rijeka, Croatia
*Corresponding author: marko.canadija@riteh.uniri.hr

Original scientific paper
Received: July 17, 2025
Accepted: October 6, 2026
https://doi.org/10.65776/ep.21.2.2

This work is licensed under a Creative Commons Attribution 3.0 Unported License.

Abstract

With the rise of machine learning (ML) in recent decades, material modeling is one of the aspects of solid mechanics that has been the subject of applications of different ML techniques over the years. The most prominent of these ML techniques, with which this work also deals with, are neural networks (NNs). They have proven to be excellent candidates for modeling relations that are difficult to capture with conventional closed-form functions providing engineers with the ability to perform numerical analyses of more complex materials with greater confidence. However, NNs are often tools that are applied in a brute force manner without further thought given to their inner workings. In this work we give an overview of the possible restrictions that can be imposed on NNs via their construction and training in order to create an NN based material model which satisfies conditions usually imposed on material models in solid mechanics. This covers restrictions such as thermodynamic consistency, objectivity, normalization of energy and stress, non-negativity of strain energy, (poly)convexity and the growth condition. These topics are covered in the context of compressible and incompressible behavior with some results shown for models commonly used for modeling rubber-like materials.

***Keywords**: hyperelasticity, physics augmented neural networks, machine learning.*

1. Introduction

Machine learning has become ever present in modern research, and recently there has been a surge of articles on the application of machine learning techniques to problems in solid mechanics and computational mechanics. The best known of these techniques are neural networks, which have become a useful tool to replace classical material models. However, the application of neural networks to solid mechanics is not new, with the first works dating back to the 1970s [1]. The field was not the focus of researchers because of the greater computational effort involved for the time, but work was nevertheless carried out on this topic. One such work dealing with the modelling of hyperelastic materials is that of [2] where the application of classical feed-forward neural networks is shown. A larger number of works has been published in recent years as machine learning libraries have become more available and easier to use, in this work all the presented examples use the TensorFlow library [3]. Some of the various applications are related to modelling rubber by predicting the stresses from strain as shown in [4] or [5], the application to metal plasticity in place of traditional return mapping algorithms [6], or by taking advantage of proper orthogonal decomposition [7]. Further examples of neural networks being used as surrogate models for finite element calculations to provide real time solutions is presented in [8] and [9]. There are of course many more works and this should not be considered an exhaustive list. However, these works all employ NNs in their most classical sense, without further adjusting the NNs to account for some physical restrictions, or just partly adjusting the loss function of the neural network. A more detailed approach is presented under the common name physics-augmented neural networks (PANNs) where the NN architecture is such that it allows the fulfillment of restrictions used in material modeling in solid mechanics such as thermodynamic consistency, objectivity, normalization of energy and stress, non-negativity of strain energy, (poly)convexity and the growth condition. There are numerous works published on this topic dealing with a range of hyperelastic materials where [10] provide a general outline to enforcing physics in PANNs, [11] describe the inclusion of additional parameters, [12] deals with application to anisotropic behavior, [13] apply PANNs in magneto-elasticity with a relaxed convexity criteria, and isotropic damage modeling was implemented in [14]. It is worth mentioning that this was a brief overview and should not be considered an exhaustive list.

In this work a guide is given on how to introduce physical constraints in modeling incompressible hyperelastic materials with feed-forward neural networks, alongside a new proposed activation function. The proposed methods are also followed by references and examples which highlight the benefits or drawbacks of certain implementations and restrictions.

2. Neural Network Architecture

Feed-forward neural networks (FNNs) are the most used NN architecture in material modeling. An illustration of a shallow neural network is given in Fig. 1 where the input layer contains the entries to an NN. The neurons within each following layer are connected to those in the previous layer with weights $w_{ij}^{[l]}$, where "l" refers to the layer index (the input layer having the numbering $l = 0$), "i" refers to the index of the neuron in the previous layer [l -

1] and "j" to the index of the neuron in the current layer. A bias value may be included to be added to every neuron and it is not tied to the inputs of the NN but is rather a standalone value. The values of a neuron within some hidden layer in an FNN can be written using

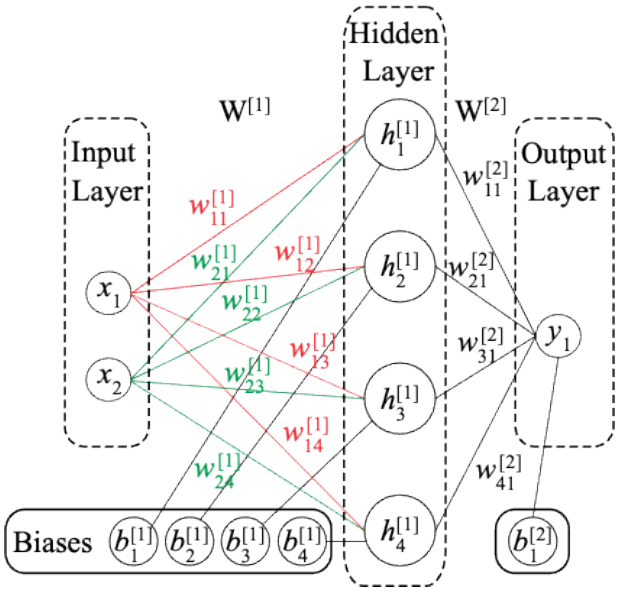


Fig. 1. Illustration of an FNN with one hidden layer and biases.

a more general formula as

$$h_j = \sum_{i=1}^{n_l} h_i w_{i,j}^{[l]} + b_j, \tag{1}$$

or if an additional activation function is to be added then the expression in Eq. (1) can be written as

$$h_j = g\left(\sum_{i=1}^{n} h_i^{[l-1]} w_{i,j}^{[l]} + b_j\right), \tag{2}$$

where $g(\cdot)$ is the activation function. The most common choice for the activation function are the sigmoid function or the hyperbolic tangent and they can also be used in material modeling as was done in [2], [4] or [5]. In the context of PANNs, the softplus function is usually chosen as in [12] or [10] for example. In this work we will consider the linear exponential function as the activation which was first proposed in [15] and applied in [14] and [16].

3. Physical Restrictions

A hyperelastic material is such a material whose behavior is defined by a strain energy function ψ. In place of an analytical expression, we use an NN as the strain energy function. The main goal is to impose the following restrictions upon the NN:

1. Objectivity,
2. Thermodynamic consistency,
3. Normalization of energy,
4. Normalization of stress,
5. Convexity or polyconvexity.

Objectivity (also called the principle of material frame-indifference) entails that the value of energy does not change under rigid body motion, i.e. if the frame of reference changes then the value of the energy should remain the same. This is ensured by using the invariants of the right Cauchy Green deformation tensor $\mathbf{C}$ as inputs to the NN. In case of incompressible behavior only the 1st and 2nd invariants are needed and they are obtained as follows:

$$\begin{aligned} I_1 &= \mathrm{tr}(\mathbf{C}) = \lambda_1^2 + \lambda_2^2 + \lambda_3^2, \\ I_2 &= \mathrm{tr}\big(\mathrm{cof}(\mathbf{C})\big) = \lambda_1^2\lambda_2^2 + \lambda_1^2\lambda_3^2 + \lambda_2^2\lambda_3^2, \end{aligned} \tag{3}$$

where λ_a $(a = 1,2,3)$ are called the principal stretches and are the eigenvalues of the right stretch tensor $\mathbf{U}$. Given that the invariants are functions of eigenvalues they do not change with a change in the reference frame. Thermodynamic consistency means that the stress tensor can be calculated by differentiating the strain energy with respect to a measure of deformation

$$\mathbf{P} = \frac{\partial \psi}{\partial \mathbf{F}}, \mathbf{S} = 2\frac{\partial \psi}{\partial \mathbf{C}}, \boldsymbol{\sigma} = 2\frac{\partial \psi}{\partial \mathbf{b}}\mathbf{b}, \tag{4}$$

where $\mathbf{P}$, $\mathbf{S}$ and $\boldsymbol{\sigma}$ are the 1st and 2nd Piola-Kirchhoff, and Cauchy stress tensors, respectively. In the context of NNs this means that the NN will be trained on stress data. Assuming incompressibility the 2nd Piola-Kirchhoff stress tensor can be calculated as

$$\mathbf{S} = 2\left[\left(\frac{\partial \psi}{\partial I_1} + I_1\frac{\partial \psi}{\partial I_2}\right)\mathbf{I} - \frac{\partial \psi}{\partial I_2}\mathbf{C}\right] - p\mathbf{C}^{-1}, \tag{5}$$

where p is a Lagrange multiplier that enforces incompressibility. From the plane stress condition $S_3 = 0$ it can be expressed as

$$p = 2\lambda_3^2\left[\frac{\partial \psi}{\partial I_1} + (\lambda_1^2 + \lambda_2^2)\frac{\partial \psi}{\partial I_2}\right], \tag{6}$$

fully defining the stress tensor and permitting the training of NNs on plane stress data assuming incompressibility. Furthermore, in the undeformed configuration where $\mathbf{C} = \mathbf{1}$(and subsequently $\lambda_1 = \lambda_2 = \lambda_3 = 1$), combining Eqs. (3), (5) and (6) lends the expression

$$\mathbf{S}_{|\mathbf{C}=\mathbf{I}} = 2\left[\left(\frac{\partial\psi}{\partial I_1} + 3\frac{\partial\psi}{\partial I_2}\right)\mathbf{I} - \frac{\partial\psi}{\partial I_2}\mathbf{I}\right] - 2\left[\frac{\partial\psi}{\partial I_1} + 2\frac{\partial\psi}{\partial I_2}\right]\mathbf{I} = \mathbf{0}, \tag{7}$$

showing that stress is always normalized, i.e. there is no stress in the undeformed configuration. Fulfilling the normalization of energy is achieved by using the proposed linear exponential activation function presented in [15]

$$g(x) = e^{\alpha \cdot x} - 1, \tag{8}$$

and by modifying the inputs to the NN to be (I_1 - 3, I_2 - 3) instead of just (I_1, I_2) so that in the undeformed state when $I_1 = I_2 = 3$ the output of the activation function is equal to zero, i.e. $g(I_1 - 3; \mathbf{C} = \mathbf{I}) = g(3 - 3) = e^{\alpha \cdot 0} - 1 = 1 - 1 = 0$. Thus, the normalization condition of energy is always satisfied. The normalization condition of energy is illustrated in Figure 2a, and the normalization of stress is illustrated in Figure 2b.

Convexity can be seen as a beneficial property since it guarantees the existence of a solution in any situation. It makes the material stable so during analysis if excessively large strains occur the analysis will not fail due to the material model. Additionally, convexity as a property helps to clear out potential noise in the dataset [16] which is useful in the context of obtaining material behavior from experimental data when high fidelity of the data cannot be guaranteed. A multivariate function is convex if Sylvester's criterion holds, if its Hessian is positive semi-definite. This is written as the following inequality

$$\boldsymbol{x}^T\mathbf{A}\boldsymbol{x} \geq 0, \qquad \forall\, x \in \mathbb{R}, \tag{9}$$

where **A** is the hessian of the function and $\boldsymbol{x}$ is a real valued vector.

In the context of the linear exponential activation function presented in Eq. (8) the individual components of the Hessian would be as follows:

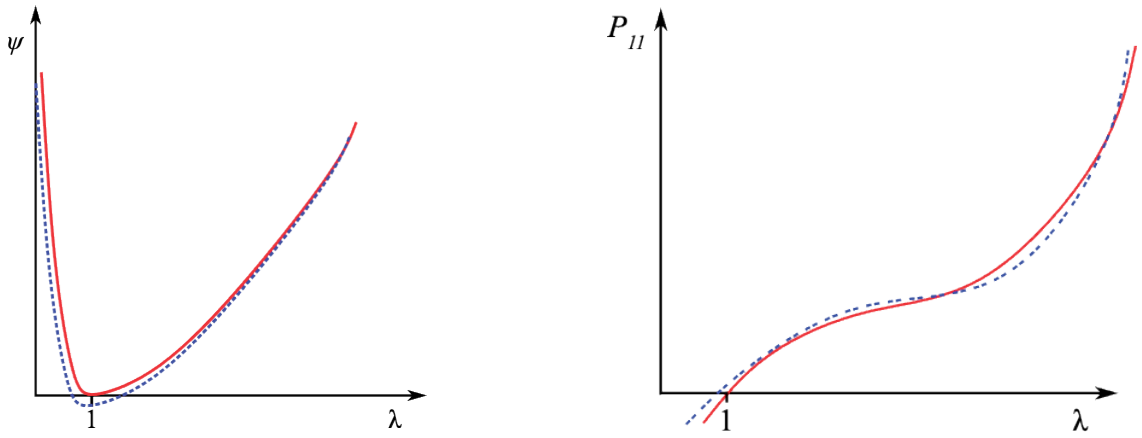
$$A_{11} = \alpha_n^2\left(w_{1,n}^{[1]}\right)^2 \exp\left\{\alpha_n\left[w_{1,n}^{[1]}(I_1 - 3) w_{2,n}^{[1]}(I_2 - 3)\right]\right\}, \tag{10}$$

$$A_{12} = \alpha_n^2 w_{1,n}^{[1]} w_{2,n}^{[1]} \exp\left\{\alpha_n\left[w_{1,n}^{[1]}(I_1 - 3) w_{2,n}^{[1]}(I_2 - 3)\right]\right\}, \tag{11}$$

$$A_{22} = \alpha_n^2\left(w_{2,n}^{[1]}\right)^2 \exp\left\{\alpha_n\left[w_{1,n}^{[1]}(I_1 - 3) w_{2,n}^{[1]}(I_2 - 3)\right]\right\}, \tag{12}$$

The inequality can be calculated using Eqs. (9), (10), (11) and (12) as

$$\begin{aligned}
&[x_1 \quad x_2]\begin{vmatrix} A_{11} & A_{12} \\ A_{12} & A_{22} \end{vmatrix}\begin{bmatrix} x_1 \\ x_2 \end{bmatrix} = \\
&x_1^2\alpha_n^2\left(w_{1,n}^{[1]}\right)^2 \exp\left\{\alpha_n\left[w_{1,n}^{[1]}(I_1 - 3)\right.\right. \\
&\left.\left. + w_{2,n}^{[1]}(I_2 - 3)\right]\right\} \\
&+ x_2^2\alpha_n^2\left(w_{2,n}^{[1]}\right)^2 \exp\left\{\alpha_n\left[w_{1,n}^{[1]}(I_1 - 3)\right.\right. \\
&\left.\left. + w_{2,n}^{[1]}(I_2 - 3)\right]\right\} \\
&+ 2x_1x_2\alpha_n^2 w_{1,n}^{[1]} w_{2,n}^{[1]} \exp\left\{\alpha_n\left[w_{1,n}^{[1]}(I_1 - 3)\right.\right. \\
&\left.\left. + w_{2,n}^{[1]}(I_2 - 3)\right]\right\} \\
&= \alpha_n^2 \exp\left\{\alpha_n\left[w_{1,n}^{[1]}(I_1 - 3) + w_{2,n}^{[1]}(I_2 - 3\right.\right. \\
&\cdot\left(x_1 w_{1,n}^{[1]} + x_2 w_{2,n}^{[1]}\right)^2.
\end{aligned} \tag{13}$$



a) Normalization of energy. **b) Normalization of stress.**

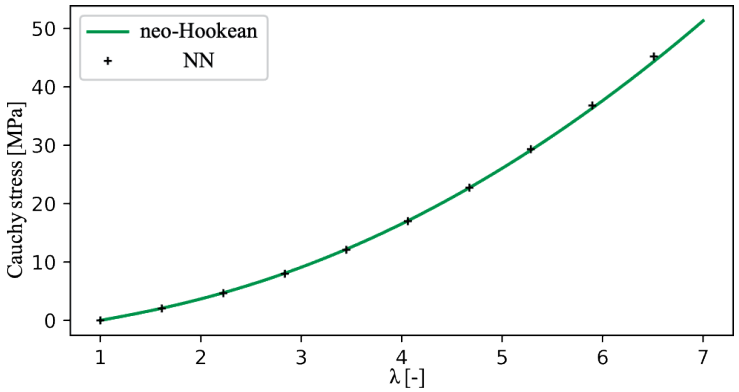
Figure 2. Illustration of normalization conditions for energy and stress. The dashed blue line represents a non-normalized model where for a stretch λ = 1 (undeformed state) the energy and stress are not zero, while the solid red line represents a normalized model.

Note that the result obtained in Eq. (13) all the individual members are positive. Meaning that the activation function is always convex with respect to the input invariants. However, the NN can be expressed as a sum of the activation functions in the hidden layer as

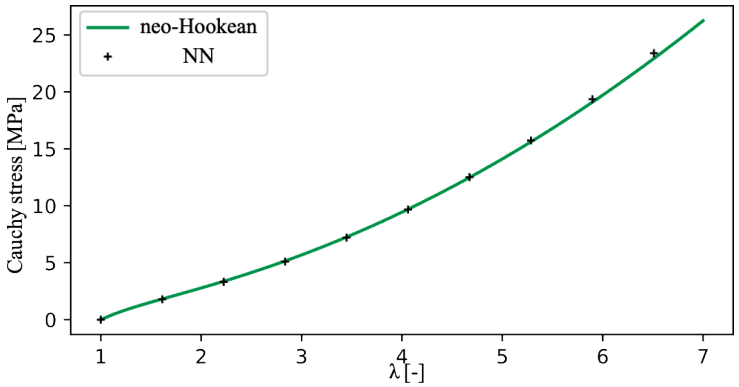
$$\psi_{\mathrm{NN}} = \sum_{i=1}^{n} g_i w_{i,1}^{[2]}. \tag{14}$$

To ensure the NN energy is a convex function the weights $w_{i,1}^{[2]}$ between the hidden layer and the output must be non-negative. A further step is to guarantee polyconvexity. Polyconvexity was proposed by [17] as an alternative condition which satisfies ellipticity and is easier to fulfil. In short, polyconvexity is a condition that guarantees the existence of a minimum but does not guarantee uniqueness of the solution. It requires that a function is convex in the deformation gradient **F**, its cofactor cof(**F**), and determinant det(**F**). If we treat and incompressible material then the convexity in det(**F**) can be left out as it defines the volume change.

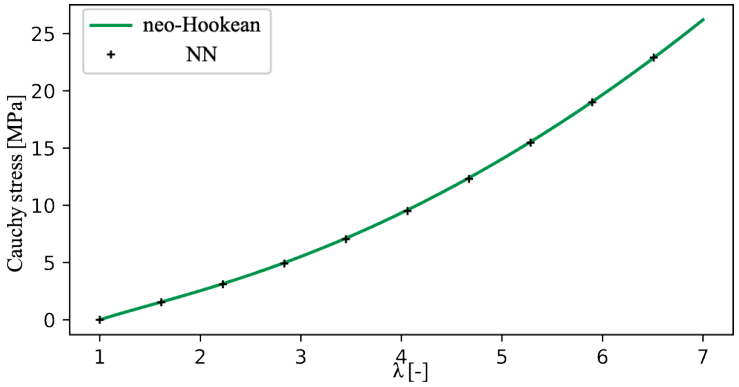
Furthermore, the invariants of the right Cauchy-Green deformation tensor **C** can be written as $I_1 = \mathbf{F}:\mathbf{F} = ||\mathrm{F}||^2$ and $I_2 = \mathrm{cof}(\mathbf{F}):\mathrm{cof}(\mathbf{F}) = ||\mathrm{cof}(\mathbf{F})||^2$. Proving polyconvexity thus means considering the convexity of a composition of functions which means that all the functions in the com-



a) Uniaxial tension – average error 3.13%.



b) Equibiaxial tension – average error 3.2%.



c) Planar tension – average error 1.9%.

Figure 3. Stress obtained by the neural network model with physical constraints, the neo-Hookean model is used to simulate experimental data. Cauchy stress is shown on the vertical axis and stretch on the horizontal axis. Uniaxial and equibiaxial tension were used during training while planar tension is used as validation of the model.

position should be convex and non-decreasing. In order to guarantee that all the functions are non-decreasing then the weights $w_{i,j}^{[1]}$ between the input and hidden layer must also be kept non-negative.

4. Numerical Example

In order to test the proposed neural network with all the included physical constraints it is applied to a material model for finite strains that is applied in describing rubber or biological behavior, the neo-Hookean model. The neo-Hookean model is widely used because of its simple form:

$$\psi_{NH} = \frac{\mu}{2}(I_1 - 3), \tag{15}$$

where μ is the shear modulus. It is used to create uniaxial, equibiaxial and planar tension data and the stress tensor is calculated as per Eq. (5). The neural network is trained on plane stress on uniaxial and equibiaxial tension and with the pressure term recovered during training as explained in Eq. (6). There were 50 training pairs per deformation mode, in total 100 training data points. The deformation gradient for incompressible behavior during uniaxial, equibiaxial and planar tension are $\mathbf{F}_{\text{uni}} = \text{diag}(\lambda, \lambda^{-1/2}, \lambda^{-1/2})$, $\mathbf{F}_{\text{equi}} = \text{diag}(\lambda, \lambda, \lambda^{-1})$, $\mathbf{F}_{\text{PT}} = \text{diag}(\lambda, 1, \lambda^{-1})$ with λ being the prescribed stretch during deformation. After training the Cauchy stress/stretch curves are shown and additionally planar tension is checked for. The results are given in Fig. 3 and show excellent agreement.

5. Conclusion

The physics augmented neural network (PANN) presented in this work shows the possibility of capturing incompressible rubber-like behavior, here simulated by the neo-Hookean model, whilst preserving the properties of objectivity, thermodynamic consistency, normalization of energy, normalization of stress, and polyconvexity. This helps ensure that structures made of such materials can be analyzed correctly and offer stability during numerical analysis.

References

[1] G. Yagawa and H. Okuda, "Neural networks in computational mechanics," *Archives of Computational Methods in Engineering*, vol. 3, no. 4, pp. 435–512, Dec. 1996, doi: 10.1007/BF02818935.

[2] Y. Shen, K. Chandrashekhara, W. F. Breig, and L. R. Oliver, "Neural Network Based Constitutive Model for Rubber Material," *Rubber Chemistry and Technology*, vol. 77, no. 2, pp. 257–277, May 2004, doi: 10.5254/1.3547822.

[3] M. Abadi *et al.*, "TensorFlow: a system for large-scale machine learning," in *Proceedings of the 12th USENIX Conference on Operating Systems Design and Implementation*, in OSDI'16. USA: USENIX Association, 2016, pp. 265–283.

[4] P. Weber, J. Geiger, and W. Wagner, "Constrained neural network training and its application to hyperelastic material modeling," *Comput Mech*, vol. 68, no. 5, pp. 1179–1204, Nov. 2021, doi: 10.1007/s00466-021-02064-8.

[5] M. Zlatić and M. Čanađija, "Incompressible rubber thermoelasticity: a neural network approach," *Comput Mech*, vol. 71, no. 5, pp. 895–916, May 2023, doi: 10.1007/s00466-023-02278-y.

[6] M. L. du Bos, F. Balabdaoui, and J. N. Heidenreich, "Modeling stress-strain curves with neural networks: a scalable alternative to the return mapping algorithm," *Comput Mater Sci*, vol. 178, p. 109629, Jun. 2020, doi: 10.1016/j.commatsci.2020.109629.

[7] D. Huang, J. N. Fuhg, C. Weißenfels, and P. Wriggers, "A machine learning based plasticity model using proper orthogonal decomposition," *Comput Methods Appl Mech Eng*, vol. 365, p. 113008, Jun. 2020, doi: 10.1016/j.cma.2020.113008.

[8] A. Mendizabal, P. Márquez-Neila, and S. Cotin, "Simulation of hyperelastic materials in real-time using deep learning," *Med Image Anal*, vol. 59, p. 101569, Jan. 2020, doi: 10.1016/j.media.2019.101569.

[9] L. Liang, M. Liu, C. Martin, and W. Sun, "A deep learning approach to estimate stress distribution: a fast and accurate surrogate of finite-element analysis," *J R Soc Interface*, vol. 15, no. 138, p. 20170844, Jan. 2018, doi: 10.1098/rsif.2017.0844.

[10] L. Linden, D. K. Klein, K. A. Kalina, J. Brummund, O. Weeger, and M. Kästner, "Neural networks meet hyperelasticity: A guide to enforcing physics," *J Mech Phys Solids*, vol. 179, p. 105363, Oct. 2023, doi: 10.1016/j.jmps.2023.105363.

[11] D. K. Klein, F. J. Roth, I. Valizadeh, and O. Weeger, "Parametrized polyconvex hyperelasticity with physics-augmented neural networks," *Data-Centric Engineering*, vol. 4, p. e25, Nov. 2023, doi: 10.1017/dce.2023.21.

[12] D. K. Klein, M. Fernández, R. J. Martin, P. Neff, and O. Weeger, "Polyconvex anisotropic hyperelasticity with neural networks," *J Mech Phys Solids*, vol. 159, p. 104703, Feb. 2022, doi: 10.1016/j.jmps.2021.104703.

[13] K. A. Kalina, P. Gebhart, J. Brummund, L. Linden, W. Sun, and M. Kästner, "Neural network-based multiscale modeling of finite strain magneto-elasticity with relaxed convexity criteria," *Comput Methods Appl Mech Eng*, vol. 421, p. 116739, Mar. 2024, doi: 10.1016/j.cma.2023.116739.

[14] M. Zlatić and M. Čanađija, "Recovering Mullins damage hyperelastic behaviour with physics augmented neural networks," *J Mech Phys Solids*, vol. 193, p. 105839, Dec. 2024, doi: 10.1016/j.jmps.2024.105839.

[15] K. Linka and E. Kuhl, "A new family of Constitutive Artificial Neural Networks towards automated model discovery," *Comput Methods Appl Mech Eng*, vol. 403, p. 115731, Jan. 2023, doi: 10.1016/j.cma.2022.115731.

[16] M. Zlatić, F. Rocha, L. Stainier, and M. Čanađija, "Data-driven methods for computational mechanics: A fair comparison between neural networks based and model-free approaches," *Comput Methods Appl Mech Eng*, vol. 431, p. 117289, Nov. 2024, doi: 10.1016/j.cma.2024.117289.

[17] J. M. Ball, "Convexity conditions and existence theorems in nonlinear elasticity," *Arch Ration Mech Anal*, vol. 63, no. 4, pp. 337–403, Dec. 1976, doi: 10.1007/BF00279992.

Alen Grebo[1,*], *Lovre Krstulović-Opara*[1]

Comparison of U-Net-based mapping from DIC-derived effective strain to infrared thermography data and from infrared thermography data to DIC-derived effective strain

[1]University of Split, Faculty of Electrical Engineering Mechanical Engineering and Naval Architecture, Ulica Ruđera Boškovića 32, 21000 Split, Croatia
*Corresponding author: agrebo@fesb.hr

Original scientific paper
Received: July 2, 2026
Accepted: October 20, 2026
https://doi.org/10.65776/ep.21.2.3

This work is licensed under a Creative Commons Attribution 3.0 Unported License.

Abstract

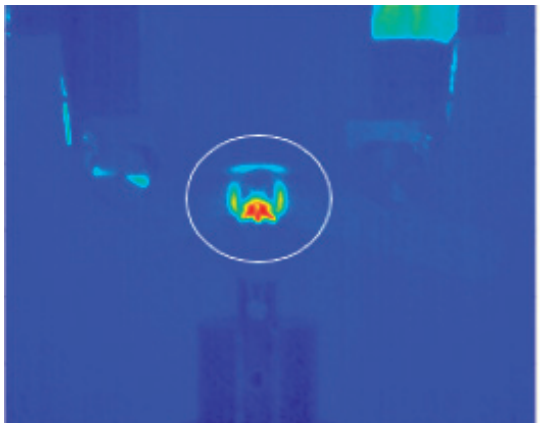
Digital Image Correlation (DIC) and Infrared Thermography (IRT) are complementary full-field techniques used in experimental mechanics for analysing deformation and thermal response during loading. Previous work demonstrated that DIC-derived effective strain fields can be used as input for U-Net-based prediction of corresponding infrared thermography fields. In this paper, that mapping direction is compared with the reverse problem, in which infrared thermography data are used to estimate DIC-derived effective strain fields. Both directions were evaluated using the same paired experimental dataset, consisting of strain and thermal fields obtained from simultaneously recorded mechanical tests. The fields were pre-processed, normalised, resized to 256 × 256 pixels, and used for supervised image-to-image regression.

The results show that both mapping directions can be learned to a certain extent using the same U-Net-based approach, but they are not equivalent. The DIC-to-IRT mapping reproduced the main thermal field distribution and showed stronger structural agreement with the reference thermographic data. The reverse IRT-to-DIC mapping achieved low average pixel-wise errors, with mean RMSE and MAE values of 0.0188 and 0.0051, respectively, but showed limited structural similarity, with a mean SSIM value of 0.0580. This indicates that thermal data contain useful information about the mechanical response, although detailed strain localisation remains difficult to reconstruct. The comparison confirms that the relationship between mechanical and thermal full-field data is direction-dependent and that thermal-to-strain estimation should be interpreted as an approximate complementary approach rather than a replacement for DIC.

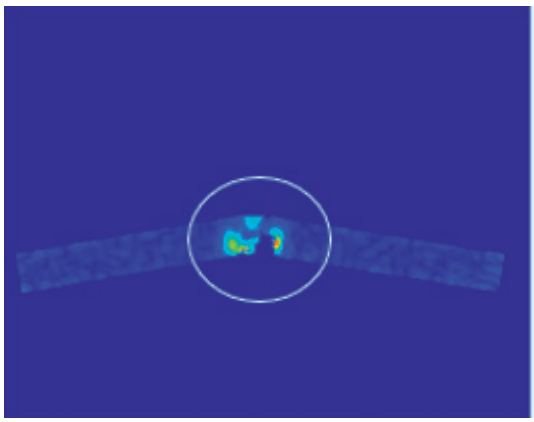
Keywords: *Digital Image Correlation; Infrared Thermography; U-Net; effective strain; image-to-image regression*

1. Introduction

Digital Image Correlation (DIC) and Infrared Thermography (IRT) are widely used full-field methods in experimental mechanics. DIC provides displacement and strain fields by tracking changes in a surface pattern during loading, while IRT records the temperature field on the specimen surface. Since mechanical deformation and thermal response often occur simultaneously, especially during localisation, plastic deformation, damage initiation, or fracture, the two techniques can provide complementary information about the same experiment as can be seen on Fig.1.



a)



b)

Fig. 1. Simultaneously acquired full-field experimental data: (a) infrared thermography image showing the surface temperature field and (b) DIC-derived effective strain field. The highlighted regions indicate the localized thermomechanical response during loading.

In many studies, DIC and IRT are used together to observe the relation between strain development and temperature changes. DIC is commonly used to identify regions of high strain, strain concentration, and crack initiation [1], while IRT can show local heating caused by thermoelastic effects, plastic dissipation, damage processes,

or heat transfer[2]. However, although both methods can be recorded at the same time, the resulting data are often treated separately. The comparison is usually made visually, through selected regions of interest, or by analysing individual time histories, rather than by directly mapping one full-field quantity to the other. Deep learning offers a possible way to study this relation in a more direct form. Convolutional neural networks, and especially encoder–decoder models such as U-Net, are suitable for image-to-image regression because they can learn spatial relations between input and output fields. This is useful in experimental mechanics, where the measured data are often available as images or full-field maps. Instead of using only selected points or averaged values, such models can be trained on paired experimental fields and used to estimate one measured quantity from another.

In previous work, a U-Net-based model was used to map DIC-derived effective strain fields to corresponding infrared thermography data [3]. This showed that, under the investigated experimental conditions, the strain field contains enough spatial information for the model to estimate the associated thermal field. However, this result only covers one mapping direction. The reverse problem is also important: whether infrared thermography data can be used to estimate the DIC-derived effective strain field.

These two problems should not be considered equivalent. Mapping from DIC-derived effective strain to IRT data asks whether the mechanical field can be used to reconstruct the thermal response. On the other hand, mapping from IRT data to DIC-derived effective strain asks whether the thermal response contains enough information to estimate the underlying mechanical field. Both tasks can be treated as image-to-image regression problems, but their physical meaning is different. The thermal field is affected by deformation, but also by heat generation, heat transfer, emissivity, surface conditions, and the time-dependent nature of the experiment. The strain field, in contrast, describes the mechanical response more directly.

The aim of this paper is therefore to compare both U-Net-based mapping directions using the same paired DIC and IRT dataset. The first model maps DIC-derived effective strain fields to infrared thermography data, while the second model maps infrared thermography data to DIC-derived effective strain fields. The comparison is based on quantitative error measures, visual agreement between predicted and reference fields, localisation of relevant regions, and the physical interpretation of the obtained results. By comparing both directions, the paper investigates whether the learned relation between mechanical and thermal full-field data is direction-dependent, and which mapping direction is more useful for experimental mechanics applications.

2. Materials and Methods

2.1. Experimental Data Acquisition

The experimental data used in this study were obtained from mechanical tests recorded simultaneously using a high-speed camera for DIC image acquisition and an infrared camera for thermographic measurements. The purpose of the acquisition setup was to obtain paired full-field mechanical and thermal data from the same specimen during loading. In this way, each DIC-derived effective strain field could be associated with the corresponding infrared thermography image.

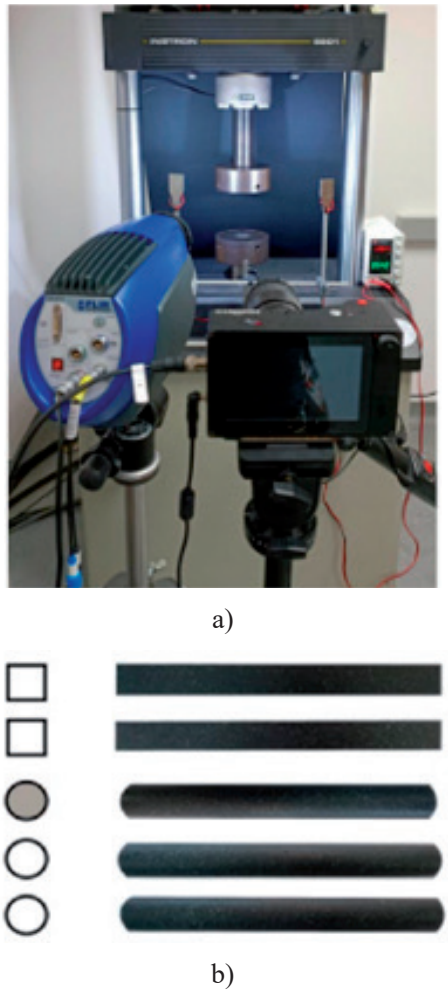


Fig. 2. Experimental setup: (a) servo hydraulic testing machine (Instron 8801, upper centre), infrared camera for temperature acquisition (FLIR SC5000MW, lower left), and high-speed camera for Digital Image Correlation measurements (Chronos 1.4, lower right); (b) aluminium alloy tube specimens, shown in empty and Ethylene–Vinyl Acetate-filled configurations.

The specimens were tested using an Instron 8801 servo-hydraulic testing machine. Loading was applied under controlled displacement conditions, with a jaw speed of 287 mm/s. During the test, the specimen surface was recorded using a Chronos 1.4 high-speed camera with a resolution of 1280 × 1024 pixels. At the same time, the thermal response of the specimen surface was recorded using a FLIR SC5000 infrared camera with a resolution of 320 × 256 pixels. Both systems were operated at a frame rate of 474 fps, allowing the rapid development of mechanical and thermal fields to be captured during loading.

For the DIC, the specimen surface seen in Fig. 2. b) was prepared with a stochastic speckle pattern suitable for op-

tical tracking [4]. The image sequence recorded by the high-speed camera was later processed to calculate displacement and strain fields. The infrared camera recorded the corresponding surface temperature field during the same loading process. Since the two systems have different spatial resolutions and measurement principles, further processing was required before the data could be used for direct full-field mapping.

2.2. Data Preprocessing

High-speed image sequences were processed using NCorr, an open-source two-dimensional local Digital Image Correlation software [5], to obtain the in-plane displacement and strain fields. The same Digital Image Correlation processing procedure and parameters as reported for this experimental dataset in our previous work [3] were used. The Eulerian–Almansi strain tensor, evaluated in the deformed configuration, was selected for strain calculation. From its normal and shear components, the two principal strains E1 and E2 were determined. An effective von Mises-type strain was subsequently adopted as the scalar measure of deformation and was calculated as:

$$E_{eff} = \sqrt{\frac{2}{3}((E_1 - E_2)^2 + E_1^2 + E_2^2)} \quad (1)$$

The resulting effective strain field was used as the mechanical full-field quantity throughout the present study. The principal NCorr processing parameters used for the five experimental datasets are summarised in Table 1.

#	1	2	3	4	5
Frames Used for DIC Processing	47	55	36	34	46
Subset Radius	16	15	17	15	16
Subset Spacing	0	0	0	0	0
Num Threads	4	4	4	4	4
Diff Norm	0.0001	0.001	0.001	0.0001	0.0001
Iterations	99	99	99	99	50
High Strain Analysis, Leap-frog Number of Steps	5	3	7	6	Off auto-propagation options
Dis-continues Analysis	On	On	On	On	On
Strain Radius	10	10	10	10	10

Table 1. NCorr analysis parameters used for each experimental dataset.

The thermographic recordings were processed to obtain the corresponding infrared thermography fields. Further processing was carried out in MATLAB. The Digital Image Correlation-derived effective strain field was used as the geometric reference for alignment. Because the optical and infrared cameras were not perfectly aligned, a small in-plane rotation was applied to the thermographic frames to correct the angular offset between the two views. The specimen region was then followed through the thermographic sequence using a specimen-centred bounding region. After cropping, the specimen was centred within the image domain so that the mechanical and thermal fields shared the same image centre. The Digital Image Correlation-derived effective strain fields were treated in the same manner, providing a common spatial reference for both modalities. The aligned fields were then resized to a common resolution of 256 × 256 pixels and stored as single-channel images. This provided spatially corresponding thermal and mechanical fields for image-to-image mapping in both directions.

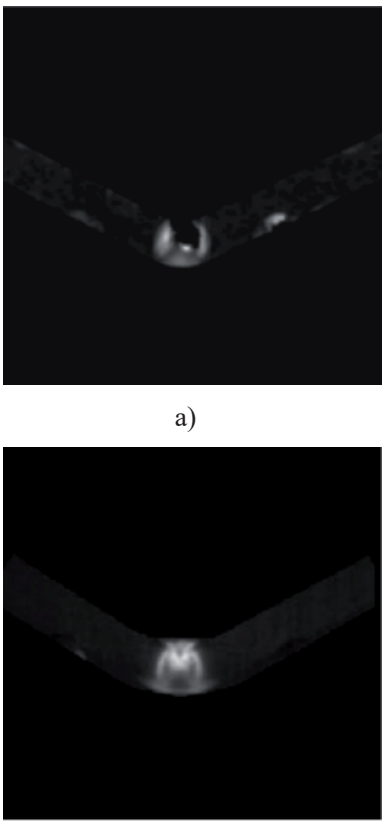
Prior to construction of the final paired dataset, the recorded sequences were screened and cleaned. Duplicate frames and non-informative frames, particularly those from the initial part of the tests before a meaningful deformation and thermal response had developed, were removed. Following this cleaning and pairing procedure, 189 corresponding Digital Image Correlation–infrared thermography image pairs remained and were used as the original dataset for model development. The data were normalised from zero to one before training to make them suitable for neural network regression. The normalisation was applied consistently within each data type.

Data set	Temperature Min	Temperature Max	Effective Strain Min	Effective Strain Max
1	19.7 °C	44.3 °C	0	4.47
2	21.1 °C	44.8 °C	0	3.96
3	20.5 °C	43.8 °C	0	4.07
4	21.3 °C	45.1 °C	0	4.34
5	20.8 °C	43.9 °C	0	4.14

Table 2. Minimum and maximum effective strain and temperature values per dataset.

The dataset consisted of 189 paired Digital Image Correlation–infrared thermography full-field images acquired from five experiments. The paired frames were divided at the individual-frame level into training, validation, and test subsets using a 70/15/15 ratio. The division was performed so that all five experiments were represented in each subset. Within each experiment, frames were also distributed across the complete loading sequence, ensuring that the training, validation, and test subsets each contained data from the early, intermediate, and later stages of deformation. The subsets were therefore not formed from separate experiments or from consecutive temporal sections of individual loading sequences. The split was performed before data augmentation, and no original image pair was repeated between subsets. Data augmentation was subsequently applied separately within each subset while preserving the spatial correspondence between the effective strain and thermographic fields. The same geometric

transformation was applied simultaneously to both images of each pair. The augmentation consisted of random rotations within ±3°, translations of up to ±5 pixels, and uniform scaling within ±3%. These transformations were selected to represent realistic image-space variations associated with small differences in camera positioning, alignment, framing and field of view, thereby reducing the dependence of the network on one exact acquisition geometry. Each original pair was augmented several times using random combinations of these transformations, with up to nine augmented versions generated from a single original pair. All augmented versions originating from a given pair remained within the same subset as the original pair, thereby preventing data leakage between the training, validation, and test sets. After augmentation, the final dataset contained 1655 paired images, comprising approximately 1158 training pairs, 248 validation pairs, and 249 test pairs. In the first direction, the DIC-derived effective strain field was used as the input and the infrared thermography image was used as the target. In the second direction, the infrared thermography image was used as the input and the DIC-derived effective strain field was used as the target. This allowed both mapping directions to be compared using the same experimental data and preprocessing procedure.



a)

b)

Fig. 3. Examples of paired input–output data used for network training: a) effective strain field obtained from DIC; b) corresponding thermal field.

2.3. U-Net Architecture and Training Strategy

A U-Net-based convolutional neural network [6] was used for both mapping directions considered in this study. The U-Net architecture was selected because it is well suited for image-to-image regression problems in which the spatial correspondence between the input and output fields must be preserved. This is particularly important for full-field experimental data, where localised regions, gradients, and spatial patterns contain relevant mechanical and thermal information.

The network follows an encoder–decoder structure. The encoder progressively extracts spatial features from the input field, while the decoder reconstructs the corresponding target field at the original image resolution. Skip connections between corresponding encoder and decoder stages transfer spatial information from the contracting path to the expanding path. These connections support the preservation of local details during reconstruction and reduce the loss of spatial information caused by successive down sampling operations.

All input and output fields were represented as single-channel images with dimensions of 256 × 256 pixels. The same U-Net architecture was used for both supervised mapping tasks to enable a direct comparison between the two mapping directions. Two models were trained independently. In the first model, the DIC-derived effective strain field was used as the input, while the corresponding infrared thermography field was used as the target. In the second model, the infrared thermography field was used as the input, while the corresponding DIC-derived effective strain field was used as the target.

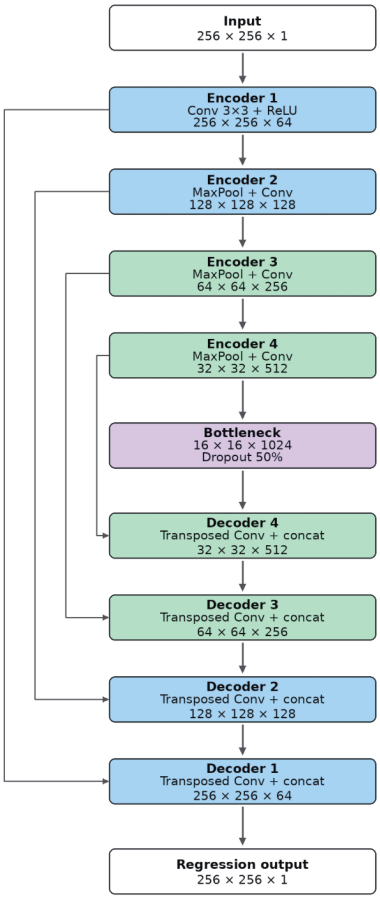


Fig. 4. Simplified schematic of the U-Net architecture used for image-to-image regression. The same encoder–decoder structure with skip connections was used for both mapping directions.

The models were implemented and trained in MATLAB using the processed paired dataset described in the previous section. Both mapping directions were trained independently using the same training configuration. The Adam optimiser was used with an initial learning rate of 1x10-4, a mini-batch size of 8, and a maximum of 400 epochs. Mean squared error was used as the loss function between the predicted field and the corresponding reference experimental field. The maximum number of epochs was used as a common upper training limit, while the training loss reached a stable region during the later stages of training. The same training procedure was applied to both mapping directions, including the same dataset division, image dimensions, input format, optimiser, learning rate, mini-batch size, number of epochs, loss function, validation strategy, and performance evaluation criteria. Consequently, the comparison was not influenced by differences in network design, data preparation, or training configuration.

Model performance was monitored using the validation subset throughout training. Following completion of the training procedure, both models were evaluated using the held-out test subset, which was not used during training. The agreement between the predicted and reference fields was quantified using Root Mean Squared Error (RMSE), Squared correlation coefficient (R2) and the Structural Similarity Index Measure (SSIM) [7]. MAE quantifies the average absolute pixel-wise difference between the predicted and reference fields, with lower values indicating smaller overall prediction error. RMSE also measures the pixel-wise prediction error, but gives greater weight to larger deviations because the errors are squared before averaging. Therefore, RMSE is more sensitive to local regions with higher prediction error. Since both MAE and RMSE are expressed in the same normalised scale as the evaluated fields, they provide a direct measure of the average reconstruction error.

SSIM evaluates the structural similarity between the predicted and reference fields by considering luminance, contrast, and spatial structure. Unlike MAE and RMSE, which are based only on pixel-wise differences, SSIM provides information about whether the spatial organisation of the reconstructed field is preserved. Values closer to 1 indicate greater structural similarity. The relationship between predicted and reference pixel values was also assessed using (R2)-based measures. The correlation-based value, (R2) was calculated as the squared correlation coefficient between the predicted and reference pixel values and describes how well both fields follow the same global trend.

The sum-of-squares-based value (R2) corresponds to the classical coefficient of determination and describes how much of the variance in the reference field is explained by the prediction. These measures were used together with MAE, RMSE, and SSIM because pixel-wise error, structural similarity, and global correlation describe different aspects of model performance. In addition to the quantitative evaluation, representative predictions were visually compared with the corresponding reference fields. This enabled the assessment of spatial distributions, gradients, and localised regions that may not be fully characterised by global numerical metrics. By using the same architecture, training strategy, and evaluation criteria for both mapping directions, the observed differences in model performance can primarily be attributed to the direction of the mapping itself.

2.4. Mapping from DIC-Derived Effective Strain to Infrared Thermography Data

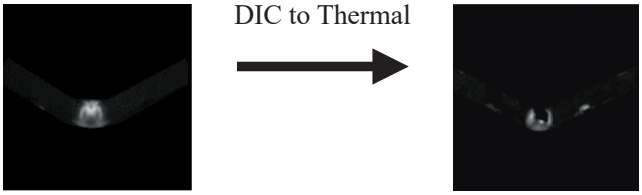
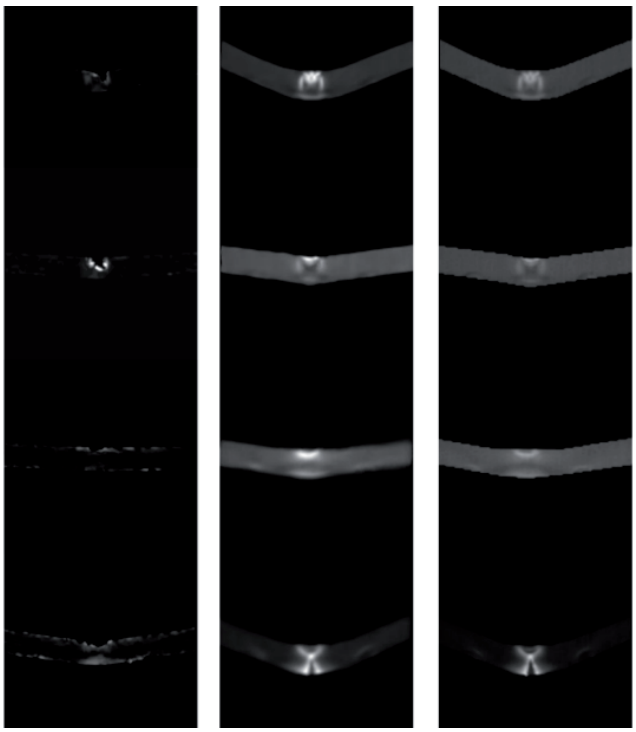


Fig. 5. Schematic representation of mapping from DIC-Derived Effective Strain to Infrared Thermography

The first mapping direction seen in Fig.6. considered in this study was the prediction of infrared thermography data from DIC-derived effective strain fields. In this configuration (see Fig. 5.), the effective strain field obtained from DIC processing was used as the input to the trained U-Net model, while the corresponding infrared thermography field was used as the reference target. This mapping direction evaluates whether the spatial information contained in the mechanical strain field can be used to reconstruct the associated thermal response of the specimen.



a) b) c)

Fig. 6. Representative results of the DIC-derived effective strain to infrared thermography mapping: a) input DIC-derived effective strain fields, b) predicted infrared thermography fields, and c) reference infrared thermography fields.

The DIC-derived effective strain to infrared thermography mapping has already been evaluated in previous work using the same general U-Net-based regression approach. The model demonstrated strong agreement between the predicted and experimentally measured thermal fields, particularly during mechanically active deformation stages, where the relationship between strain localisation and temperature variation was more pronounced.

The global test-set evaluation reported an RMSE of 0.0986, MAE of 0.0561, SSIM of 0.4262, and R^2 of 0.968. A pixel-level comparison between predicted and reference thermal fields also showed high agreement, with R^2 values of 0.985, 0.966, and 0.968 depending on the number of sampled datapoints.

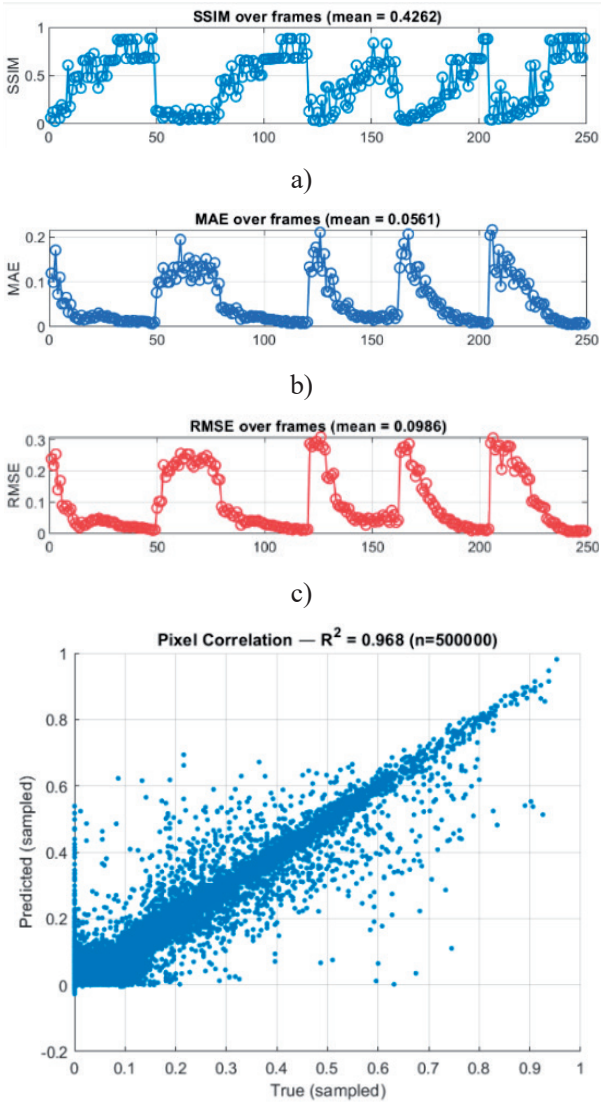


Fig.7. Quantitative evaluation of the DIC-derived effective strain to infrared thermography mapping: a) SSIM over frames, b) MAE over frames, c) RMSE over frames, and d) pixel-wise correlation between reference and predicted thermographic fields.

The results shown on Fig.7.indicate that the U-Net model was able to reproduce the dominant spatial features of the thermographic response from the DIC-derived effective strain field. The predicted thermal fields preserved the main specimen geometry and captured the regions associated with thermally active deformation. This confirms that the effective strain field contains relevant spatial information related to the thermal response under the investigated loading conditions.

However, the prediction accuracy was not uniform throughout the loading sequence. The highest errors were observed in the initial frames, where both the strain field and the thermal field contained limited spatial structure. In these nearly uniform states, the mapping between the mechanical and thermal fields is weakly defined, and small absolute deviations can produce comparatively large normalised errors. In the earliest frames, RMSE values of approximately 0.24–0.26 were reported. As deformation developed and localisation became more pronounced, the prediction accuracy improved considerably.

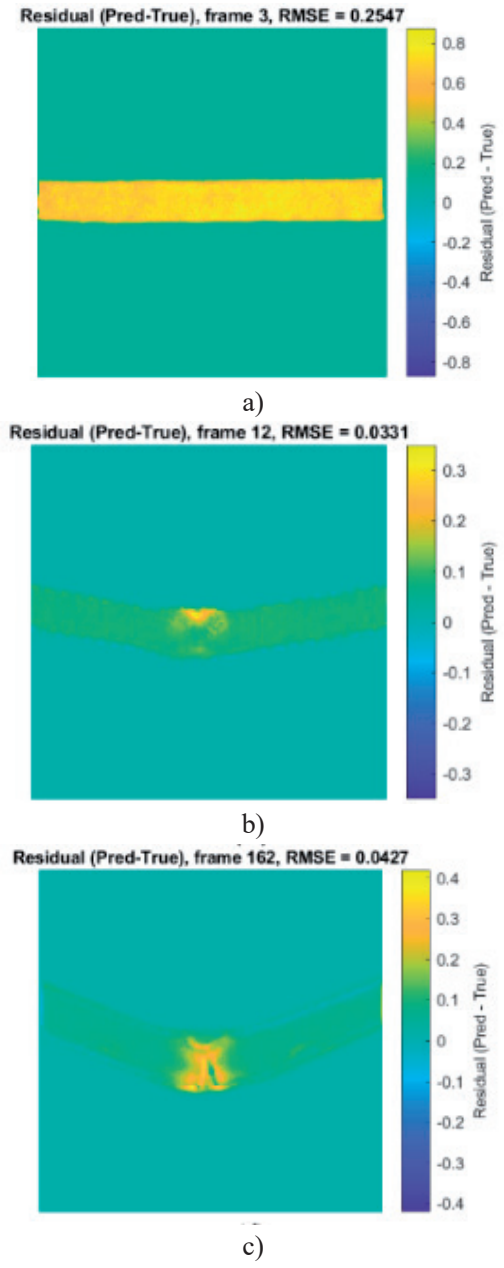


Fig.8. Residual error maps for the DIC-derived effective strain to infrared thermography mapping at selected frames: a) frame 3, b) frame 12, and c) frame 162. The residuals are calculated as the difference between the predicted and reference fields.

During the mechanically relevant part of the test sequence, approximately between frames 6 and 50, the reported MAE stabilised around 0.01–0.03, RMSE decreased to approximately, 0.02–0.04 and SSIM reached values of approximately 0.6–0.8. This behaviour indicates that the model performed best when the thermomechanical response contained clear spatial features related to deformation and damage development. Residual maps seen on Fig.8. show that the remaining discrepancies were mainly concentrated near regions with steep thermal gradients and localised deformation. These regions are expected to be more difficult to reconstruct because small spatial misalignments or local DIC noise can result in visible differences between predicted and measured thermal fields. Nevertheless, the residual fields did not indicate systematic artefacts, suggesting that the model learned a consistent relationship between the paired strain and thermal fields within the investigated experimental domain.

Overall, the DIC-derived effective strain to infrared thermography mapping demonstrated that a U-Net-based regression model can estimate the main thermal field distribution from mechanical full-field data. The results also show that the quality of the prediction depends strongly on the amount of meaningful spatial information present in the input and target fields. The mapping is most reliable during deformation stages where strain localisation and thermal response are clearly developed, while the initial nearly uniform frames remain more difficult to predict. These findings provide the reference basis for comparison with the reverse mapping direction, in which infrared thermography data are used to estimate DIC-derived effective strain fields.

2.5. Mapping from Infrared Thermography Data to DIC-Derived Effective Strain

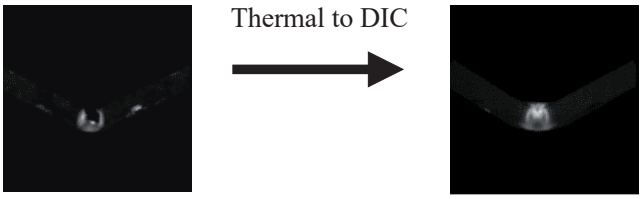


Fig. 9. Schematic representation of mapping from infrared thermography data to DIC-derived effective strain.

The second mapping direction considered (see Fig.9.) in this study was the estimation of DIC-derived effective strain fields from infrared thermography data. In this configuration, the thermographic field was used as the input to the trained U-Net model, while the corresponding DIC-derived effective strain field was used as the reference target. This mapping direction evaluates whether the thermal response of the specimen contains sufficient spatial information to estimate the underlying mechanical strain distribution.

The trained model was applied to the held-out test subset. For each test example, the network generated a predicted effective strain field from the corresponding infrared thermography image. The predicted field was then compared with the DIC-derived reference field from the same time frame. Obtained results seen on Fig. 10. show that the U-Net model was able to estimate the general distribution of the DIC-derived effective strain field from the thermographic input. The predicted fields reproduced the overall specimen response and followed the main spatial trends observed in the reference strain fields. This indicates that the infrared thermography data contain information related to the mechanical deformation field under the investigated loading conditions.

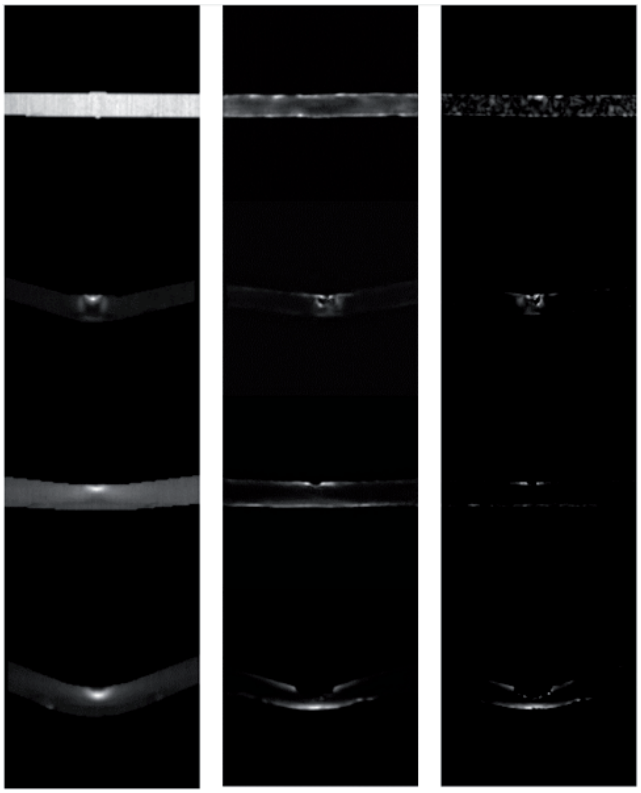
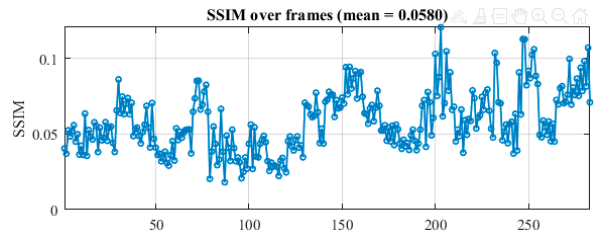


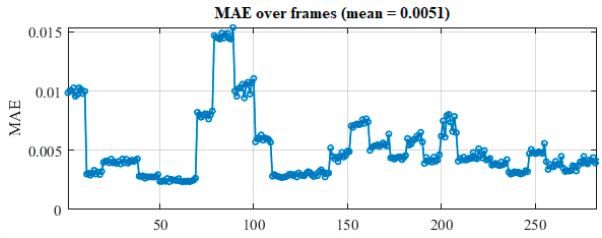
Fig. 10. Representative results of the infrared thermography to DIC-derived effective strain mapping: a) input infrared thermography fields, b) predicted DIC-derived effective strain fields, and c) reference DIC-derived effective strain fields.

The numerical evaluation seen on Fig.11. showed that the average prediction error remained relatively low. The mean RMSE over the analysed frames was 0.0188, while the mean MAE was 0.0051. The frame-wise error curves indicate that the prediction error was not constant throughout the sequence, with increased errors observed in specific frame intervals. These intervals correspond to parts of the test sequence where the strain distribution changed more rapidly or where the thermal information was less directly representative of the effective strain field. The global sampled-pixel comparison also showed a clear positive relationship between the predicted and reference DIC-derived effective strain values. For 600000 sampled pixels, the correlation-based coefficient of determination was R^2=0.692. This value indicate that the model captured a substantial part of the global relationship between the thermographic input and the corresponding mechanical strain response.

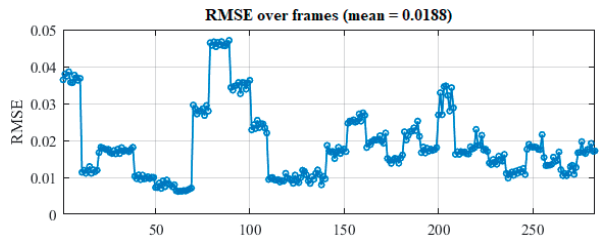
The SSIM values were considerably lower than might be expected from the pixel-wise error metrics, with a mean



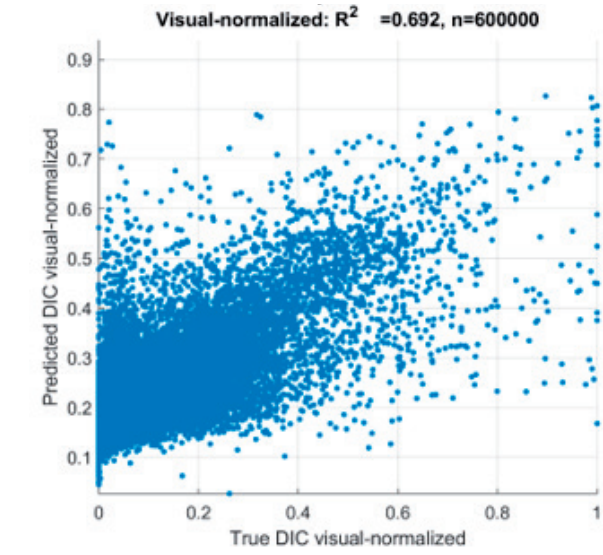
a)



b)



c)



d)

Fig.11. Quantitative evaluation of the infrared thermography to DIC-derived effective strain mapping: a) SSIM over frames, b) MAE over frames, c) RMSE over frames, and d) pixel-wise correlation between reference and predicted DIC-derived effective strain fields.

value of 0.0580 over the analysed frames. Although the model achieved relatively low average pixel-wise errors, the predicted fields did not fully reproduce the structural details of the DIC-derived effective strain fields. This difference is not contradictory, as the metrics evaluate different aspects of the prediction. RMSE and MAE quantify the average magnitude of the pixel-wise error over the complete field, whereas SSIM is more sensitive to local spatial structure, contrast, and the arrangement of features. Consequently, the model can reproduce the general strain magnitude and broad spatial distribution while still obtaining a low SSIM if narrow localisation zones are shifted, widened, smoothed, or predicted with lower peak strain values than the reference field.

A further contribution to this behaviour is the tendency of the U-Net reconstruction to smooth local features, which was also observed in the opposite mapping direction. This smoothing has a comparatively limited influence on the overall pixel-wise error but can substantially affect the structural similarity of fields containing sharp gradients and narrow strain-localisation zones. This effect is particularly important for the thermal-to-DIC mapping, since the target effective strain fields contain more sharply localised features than the comparatively smoother thermographic input fields.

The residual map for frame 142 in Fig. 12 shows that the prediction error is mainly concentrated within the specimen region, while the surrounding background remains close to zero. This indicates that the model does not introduce significant artefacts outside the mechanically relevant area. The largest residuals occur near the central deformation/localisation zone, where the DIC-derived effective strain field contains sharper gradients and more localised features. The presence of neighbouring positive and negative residual regions suggests that part of the error is related to small spatial mismatches between the predicted and reference strain distributions rather than to a uniform overprediction or underprediction. Overall, the residual map confirms that the thermal-to-DIC model captures the general strain pattern but has difficulty reproducing localised strain details with high spatial accuracy.

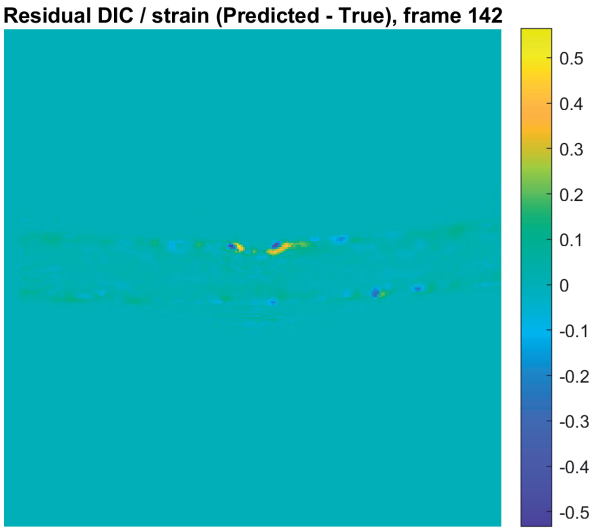


Fig.12. Residual error map for the infrared thermography to DIC-derived effective strain mapping at frame 142. The residual is calculated as the difference between the predicted and reference strain fields.

Overall, the infrared thermography-to-DIC-derived effective strain mapping demonstrated that a U-Net-based model can estimate the main mechanical strain distribution from thermal full-field data. The relatively low RMSE and

MAE values indicate good average pixel-wise agreement, while the low SSIM values show that the reconstruction of detailed spatial strain structures remains challenging. The predicted fields can therefore be considered representative of the general mechanical response and broad strain distribution, but not as quantitatively accurate reconstructions of local strain concentrations. In particular, the method should not be considered a replacement for direct DIC measurements where accurate peak strain values, strain gradients, or the detailed geometry of localisation zones are required. The results nevertheless indicate that the thermal field contains useful information about the mechanical response, while also confirming that the reverse mapping is limited by the indirect and non-unique relationship between temperature evolution and effective strain localisation

2.6. Comparison of Both Mapping Directions

The two mapping directions were compared in order to evaluate whether the learned relationship between DIC-derived effective strain fields and infrared thermography data is direction-dependent. Although both models were based on the same U-Net architecture and trained using paired full-field data, the two tasks are not physically equivalent. The first direction estimates the thermal response from a mechanical strain field, while the second direction estimates the mechanical strain field from the measured thermal response. Therefore, the comparison must consider not only numerical accuracy, but also spatial reconstruction quality and physical interpretability.

2.6.1. Quantitative Comparison

The DIC-derived effective strain to infrared thermography mapping showed strong global agreement in the previously reported evaluation, with RMSE = 0.0986, MAE = 0.0561, SSIM = 0.4262, and R^2 = 0.968 on the independent test set. During the mechanically active part of the sequence, where deformation and temperature localisation were more pronounced, the model performance improved considerably, with RMSE values decreasing to approximately 0.01–0.03, MAE values stabilising around 0.02–0.04, and SSIM values reaching approximately 0.6–0.8.

For the reverse mapping direction, from infrared thermography data to DIC-derived effective strain, the mean RMSE over the analysed frames was 0.0188 and the mean MAE was 0.0051. The global sampled-pixel comparison produced R^2=0.692 for 600000 sampled pixels. However, the mean SSIM was substantially lower, with a value of 0.0580, indicating limited structural similarity between the predicted and reference effective strain fields.

Mapping direction	RMSE	MAE	SSIM	R^2
DIC to Thermal	0.0986	0.0561	0.4262	0.968
Thermal to DIC	0.0188	0.0051	0.0580	0.692

Table 3. Quantitative comparison of the DIC-derived effective strain to infrared thermography and infrared thermography to DIC-derived effective strain mapping directions.

Although the thermal-to-DIC mapping produced lower RMSE and MAE values, these values should not be interpreted as a direct indication that this direction is superior. The two models predict different physical quantities with different spatial distributions, dynamic ranges, and normalisation behaviour. Therefore, RMSE and MAE are useful for evaluating each model individually, but they are not fully equivalent across mapping directions. A more meaningful comparison is obtained by considering the complete set of metrics together with the visual agreement between predicted and reference fields.

2.6.2. Qualitative Comparison

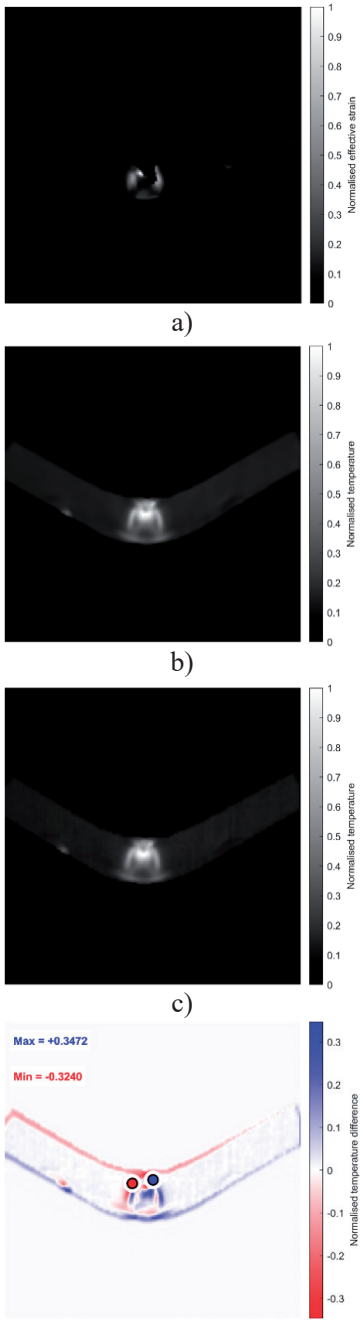


Fig.13. Representative DIC-to-thermal mapping result: a) DIC-derived effective strain input, b) predicted thermographic field, c) reference thermographic field, and d) difference between the predicted and reference thermographic fields.

Visual comparison provides additional insight into the behaviour of both models. In the DIC-derived effective strain to infrared thermography mapping on Fig.6., the predicted thermal fields reproduced the general thermal distribution and the dominant regions of temperature variation.

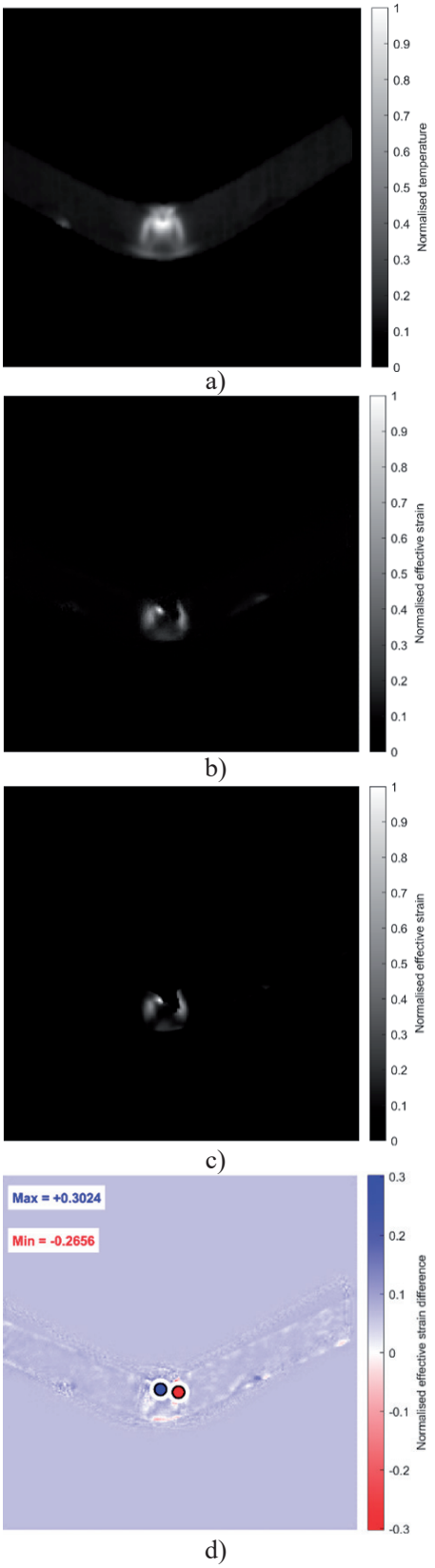


Figure 14. Representative thermal-to-DIC mapping result: a) infrared thermography input, b) predicted DIC-derived effective strain field, c) reference DIC-derived effective strain field, and d) difference between the

The model was particularly effective in frames in which deformation localisation produced a clear thermal response. To examine the behaviour in the region of significant deformation in more detail, Fig. 13. presents a representative DIC input together with the predicted and reference thermal fields and their difference map. The predicted and reference fields are shown using identical normalised colour-scale limits, allowing their spatial distributions and magnitudes to be compared directly. The model reproduces the position and broader extent of the central thermal response, while the main residuals remain concentrated around this localisation region. For the presented frame, the maximum positive and negative differences are approximately +0.347 and −0.324, respectively. The neighbouring positive and negative residuals indicate local differences in the magnitude and spatial extent of the predicted thermal response rather than a uniform over- or underprediction across the specimen. Outside the principal localisation region, the differences are considerably smaller. This confirms that the model captures the broader thermal response well, while the largest errors occur in regions characterised by steep spatial gradients and strongly localised deformation.

In the reverse mapping direction shown in Fig. 14, the model was able to estimate the general distribution of the DIC-derived effective strain field from the thermographic input. However, the reconstruction of fine localised strain features was more challenging. This is reflected in the low SSIM values, which indicate limited structural similarity between the predicted and reference strain fields despite relatively low average pixel-wise errors. The predicted fields therefore captured the broader deformation trend more reliably than the detailed strain localisation pattern. A more detailed comparison of a representative high-deformation frame is presented in Fig. 14. The predicted field reproduces the characteristic V-shaped distribution of the specimen and correctly identifies the central region in which the highest strain localisation occurs. The difference map nevertheless reveals a predominantly light-blue residual over much of the field, corresponding approximately to a positive difference of 0.05–0.10 on the normalised scale. This indicates a slight general tendency of the model to overpredict the effective strain magnitude. More pronounced discrepancies are concentrated around the central deformation region, where the maximum positive and negative differences reach approximately +0.302 and −0.266, respectively. Importantly, the residual pattern largely follows the geometry of the specimen rather than appearing randomly throughout the image. The neighbouring positive and negative extrema around the central region indicate differences in the precise position, width and magnitude of the reconstructed strain concentration. Thus, the model retains the overall shape and location of the mechanical response, while reconstruction of the sharp local strain distribution remains less accurate.

The difference between the two mapping directions is therefore important. Thermal fields are generally smoother and more spatially continuous than DIC-derived effective strain fields. As a result, predicting a thermal field from a strain input may be more favourable for an encoder–decoder network because the target distribution contains broader gradients and fewer sharply localised details. In

contrast, DIC-derived effective strain fields can contain narrow localisation zones, high-gradient regions and local variations introduced by DIC processing. These features are more difficult to reconstruct from thermal data alone.

An additional factor is the difference in the native spatial resolution and information content of the two measurement modalities. The DIC-derived strain fields originate from higher-resolution optical images, whereas the thermographic measurements were acquired at a lower spatial resolution and exhibit smoother spatial variations. Although both modalities were resized to 256 × 256 pixels before training, this resizing does not recover fine spatial information that was absent from the original thermographic measurements. Consequently, the DIC-to-thermal mapping transforms a comparatively detailed mechanical field into a smoother thermal field, whereas the reverse direction requires the model to infer finer local strain features from a spatially coarser thermal representation. This asymmetry provides an additional explanation for the greater difficulty observed in the thermal-to-DIC mapping.

2.6.3. Physical Interpretability

The comparison also shows that the two mapping directions have different physical interpretations. Mapping from DIC-derived effective strain to infrared thermography data investigates whether the mechanical deformation field contains sufficient information to estimate the corresponding thermal response. This direction is physically meaningful because local deformation, plastic dissipation, and damage development can contribute to temperature changes. However, the thermal field is also influenced by heat transfer, emissivity, surface conditions, camera response, and temporal effects. Therefore, the thermal response cannot be considered a unique function of the instantaneous strain field alone.

The reverse direction, from infrared thermography data to DIC-derived effective strain, has a different interpretation. It investigates whether the measured thermal response can be used to infer the underlying mechanical strain field. This is a more indirect problem, because temperature variations are a consequence of several coupled processes and do not uniquely define the mechanical state. The obtained results show that the thermal field contains useful information about the mechanical response, but the low SSIM values suggest that detailed strain localisation cannot be fully reconstructed from thermal data alone under the present conditions.

The comparison therefore indicates that the relationship between DIC-derived effective strain and infrared thermography data is not symmetric from a data-driven perspective. The DIC-to-IRT model showed stronger structural agreement for reconstructing the thermal field, while the IRT-to-DIC model achieved low average pixel-wise errors but weaker structural similarity. This suggests that the mapping direction strongly affects both the numerical performance and the physical meaning of the predicted field.

2.6.4. Practical Relevance

From a practical point of view, both mapping directions have potential applications, but they address different experimental needs. The DIC-derived effective strain to infrared thermography mapping may be useful in cases where thermal information is unavailable, incomplete, or difficult to acquire. If a model has been trained for a specific material, geometry, and loading configuration, it may provide an estimate of the expected thermal field based on DIC-derived mechanical data.

The infrared thermography to DIC-derived effective strain mapping is particularly interesting because it explores the possibility of estimating mechanical full-field information from thermal measurements. This may be relevant in experimental setups where conventional DIC is difficult to apply, for example due to limited optical access, poor lighting conditions, speckle pattern degradation, or camera placement restrictions. In such cases, thermal imaging could provide an indirect source of information about the mechanical response.

However, the present results indicate that thermal-to-DIC mapping should be interpreted with caution. The model can estimate the general strain distribution, but the reconstruction of detailed localised strain structures remains limited. Therefore, this approach should not be considered a direct replacement for DIC. Instead, it may be more appropriate as a complementary method for approximate strain-field estimation, experimental screening, or multimodal data fusion.

2.6.5. Limitations

Several limitations must be considered when interpreting the comparison. First, both models were trained and evaluated using data from the same experimental framework. The learned mappings are therefore specific to the investigated material, specimen geometry, loading configuration, acquisition setup, and preprocessing procedure. Generalisation to other experimental conditions cannot be assumed without additional validation.

Second, the two mapping directions predict different target quantities. Direct comparison of RMSE and MAE values is therefore limited, even when the data are normalised. The metrics are useful for assessing prediction quality within each task, but they do not provide a complete measure of physical equivalence between the two models.

Third, the thermal and strain fields differ in spatial character. Thermographic fields are generally smoother, while DIC-derived effective strain fields may contain sharper gradients, localisation zones, and processing-related noise. This difference affects SSIM and visual reconstruction quality, particularly in the thermal-to-DIC direction.

Finally, both mappings are data-driven and do not explicitly include the governing thermomechanical equations. The models learn statistical relationships between paired fields, but they do not enforce heat transfer, material constitutive behaviour, or energy balance. Future work should therefore include larger datasets, additional loading cases, temporal modelling, and physics-informed constraints in order to improve generalisation and physical consistency.

3. Conclusion

This paper compared two U-Net-based mapping directions between DIC-derived effective strain fields and infrared thermography data. The first direction used effective strain fields as input to predict thermographic fields, while the second used thermographic fields as input to estimate effective strain fields. Both models were evaluated using the same paired experimental dataset and the same general network architecture.

The results show that both directions can be learned to a certain extent, but they are not equivalent. The DIC-to-IRT mapping reproduced the main thermal field distribution and showed stronger structural agreement with the reference thermographic data. This indicates that the DIC-derived effective strain field contains relevant spatial information associated with the measured thermal response.

The reverse mapping, from IRT to DIC-derived effective strain, also produced useful estimates of the mechanical field. The model achieved low average pixel-wise errors, with mean RMSE and MAE values of 0.0188 and 0.0051, respectively. However, the low mean SSIM value shows that the detailed spatial structure of the strain field was not fully reconstructed. Therefore, this direction is better interpreted as an approximate estimation of the general strain distribution rather than a full replacement for DIC.

Overall, the comparison confirms that the relationship between mechanical and thermal full-field data is direction-dependent. The DIC-to-IRT direction is more suitable for reconstructing smoother thermographic fields, while the IRT-to-DIC direction is more challenging because strain fields contain sharper localisation zones and stronger spatial gradients. Future work should include larger datasets, additional loading cases, and temporal or physics-informed models to improve the generalisation and physical consistency of the learned mappings.

4. References

[1] B. Pan, K. Qian, H. Xie, and A. Asundi, “Two-dimensional digital image correlation for in-plane displacement and strain measurement: a review,” *Meas. Sci. Technol.*, vol. 20, no. 6, p. 62001, Apr. 2009, doi: 10.1088/0957-0233/20/6/062001.

[2] A. Chrysochoos, “Infrared thermography applied to the analysis of material behavior: a brief overview,” *Quant. Infrared Thermogr. J.*, vol. 9, no. 2, pp. 193–208, 2012, doi: 10.1080/17686733.2012.746069.

[3] A. Grebo, N. Novak, B. Panić, and L. Krstulović-Opara, “A Deep Learning Framework for Full-Field Thermal Field Distribution Prediction from Digital Image Correlation Strain Measurements,” *Applied Sciences*, vol. 16, no. 1, 2026, doi: 10.3390/app16010460.

[4] D. Lecompte *et al.*, “Quality assessment of speckle patterns for digital image correlation,” *Opt. Lasers Eng.*, vol. 44, no. 11, pp. 1132–1145, Nov. 2006, doi: 10.1016/j.optlaseng.2005.10.004.

[5] J. Blaber, B. Adair, and A. Antoniou, “Ncorr: Open-Source 2D Digital Image Correlation Matlab Software,” *Exp. Mech.*, vol. 55, no. 6, pp. 1105–1122, Jul. 2015, doi: 10.1007/s11340-015-0009-1.

[6] P. and B. T. Ronneberger Olaf and Fischer, “U-Net: Convolutional Networks for Biomedical Image Segmentation,” in *Medical Image Computing and Computer-Assisted Intervention – MICCAI 2015*, J. and W. W. M. and F. A. F. Navab Nassir and Hornegger, Ed., Cham: Springer International Publishing, 2015, pp. 234–241.

[7] Zhou Wang, A. C. Bovik, H. R. Sheikh, and E. P. Simoncelli, “Image quality assessment: from error visibility to structural similarity,” *IEEE Transactions on Image Processing*, vol. 13, no. 4, pp. 600–612, Apr. 2004, doi: 10.1109/TIP.2003.819861.

59th Annual General Assembly of the Croatian Academy of Engineering

On June 8, 2026, the 59th Annual Assembly of the Croatian Academy of Engineering (HATZ) was held at the University of Zagreb Faculty of Chemical Engineering and Technology. The Assembly consisted of a working session and a formal ceremony.

During the working session, members were informed about the Academy's financial operations, as well as the activities and results of HATZ during the 2022–2026 mandate period. The new Governing Board of the Academy for the 2026–2030 mandate period was presented, along with the newly elected department secretaries and deputy department secretaries.

The new Governing Board for the 2026–2030 mandate period consists of:

- Prof. Bruno Zelić, PhD, President;
- Prof. Neven Duić, PhD, Vice-President;
- Prof. Jana Žiljak Gršić, PhD, Vice-President;
- Assoc. Prof. Mario Bačić, PhD, Secretary-General; and
- Prof. Emeritus Vedran Mornar, PhD, Member of the Governing Board.

The newly elected department secretaries and deputy department secretaries are:

HATZ Department	Department Secretary	Deputy Department Secretary
Department of Architecture and Urban Planning	Assoc. Prof. Željka Jurković, PhD	Prof. Karin Šerman, PhD
Department of Bioprocess Engineering	Prof. Blaženka Kos, PhD	Prof. Drago Šubarić, PhD
Department of Electrical Engineering and Electronics	Prof. Josip Lorincz, PhD	Prof. Damir Sumina, PhD
Department of Energy Systems	Prof. Emeritus Zvonimir Guzović, PhD	Prof. Damir Šljivac, PhD
Department of Civil Engineering and Geodesy	Assoc. Prof. Mario Bačić, PhD	Prof. Mladen Zrinjski, PhD
Department of Graphic Engineering	Prof. Ivana Bolanča Mirković, PhD	Prof. Jana Žiljak Gršić, PhD
Department of Information Systems	Prof. Dinko Begušić, PhD	Prof. Domagoj Jakobović, PhD
Department of Chemical Engineering	Prof. Nenad Bolf, PhD	Prof. Gordana Matijašić, PhD
Department of Communication Systems	Prof. Snježana Rimac-Drlje, PhD	Prof. Mario Muštra, PhD
Department of Transport	Prof. Borna Abramović, PhD	Prof. Edouard Ivanjko, PhD
Department of Mining and Metallurgy	Prof. Mario Dobrilović, PhD	Prof. Zdenka Zovko Brodarac, PhD
Department of Mechanical Engineering and Naval Architecture	Prof. Lovre Krstulović-Opara, PhD	Prof. Nastia Degiuli, PhD
Department of Systems and Cybernetics	Prof. Andrej Jokić, PhD	Prof. Mato Baotić, PhD
Department of Textile Technology	Prof. Snježana Firšt Rogale, PhD	Prof. Željko Penava, PhD

Reports were also presented on the Academy's publishing activities, including a special presentation of the new 2025 edition of the HATZ Annual. The Annual contains 17 scientific, professional, and review papers by Academy members addressing the application of artificial intelligence in technical and biotechnical sciences.

During the formal ceremony, diplomas were presented to the newly elected Members Emeriti, Full Members of the Academy, Members of the Economic Council, and representatives of the new Supporting Members. The Academy's 2025 awards were also presented to their recipients.

The Assembly was attended by Academy members and distinguished representatives of the scientific and business communities. The participants were welcomed by Prof. Ernest Meštrović, PhD, Vice-Dean for Business Affairs at the University of Zagreb Faculty of Chemical Engineering and Technology, and Mr. Luka Jelić, President of the Croatian Engineering Association (HIS).

The status of HATZ Member Emeritus was awarded to:

- Prof. Emerita Jagoda Šušković, PhD, from the Department of Bioprocess Engineering;
- Prof. Muhamed Sućeska, PhD, from the Department of Chemical Engineering;

- Prof. Karolj Skala, PhD, from the Department of Communication Systems;
- Prof. Dragan Čišić, PhD, from the Department of Transport;
- Prof. Tonči Mikac, PhD, from the Department of Mechanical Engineering and Naval Architecture;
- Prof. Zdravko Virag, PhD, from the Department of Mechanical Engineering and Naval Architecture;
- Prof. Vladimir Medved, PhD, from the Department of Systems and Cybernetics;
- Prof. Emeritus Nedjeljko Perić, PhD, from the Department of Systems and Cybernetics; and
- Prof. Emeritus Darko Ujević, PhD, from the Department of Textile Technology.

The status of HATZ Full Member was awarded to:

- Prof. Zoran Veršić, PhD, from the Department of Architecture and Urban Planning;
- Prof. Đurđica Ačkar, PhD, from the Department of Bioprocess Engineering;
- Prof. Damir Šljivac, PhD, from the Department of Energy Systems; and
- Prof. Martin Žagar, PhD, from the Department of Information Systems.

The status of Member of the HATZ Economic Council was awarded to:

- Siniša Krajnović, PhD, President of the Governing Board of Ericsson Nikola Tesla d.d.;
- Zdravko Mužek, MSc, Director of Ekonerg holding d.o.o.; and
- Krešimir Paić, BSc, Director of ECCOS Inženjering d.o.o.

The status of HATZ Supporting Member was granted to the following companies:

- ECCOS Inženjering d.o.o.;
- Ekonerg d.o.o.;
- Ericsson Nikola Tesla d.d.; and
- ITCR d.o.o.

The Croatian Academy of Engineering Awards for 2025 were also presented at the Assembly.

The Lifetime Achievement Award "Power of Knowledge" was presented to Prof. Franjo Jović, PhD, from the Department of Systems and Cybernetics, in recognition of his outstanding contribution to the work of the Academy, his lifelong scientific research in engineering sciences, and his longstanding contribution to the advancement of the profession, with particular emphasis on the application of research results.

The Annual Awards "Rikard Podhorsky" were presented to Prof. Borna Abramović, PhD, from the Department of Transport; Prof. Nastia Degiuli, PhD, from the Department of Mechanical Engineering and Naval Architecture; and Prof. Mario Vašak, PhD, from the Department of Systems and Cybernetics. The awards recognize distinguished scientists for particularly valuable scientific and professional achievements with practical applications, contributions to improved cooperation with industry, as well as outstanding contributions to the work of the Academy and its international recognition over the past five years.

The Awards for Young Scientists "Vera Johanides" were presented to Tomislav Antić, PhD, from the University of Zagreb Faculty of Electrical Engineering and Computing; Filip Jukić, PhD, from the University of Zagreb Faculty of Electrical Engineering and Computing; Assist. Prof. Mišo Jurčević, PhD, from the University of Split Faculty of Electrical Engineering, Mechanical Engineering and Naval Architecture; and Matej Žnidarec, PhD, from the Josip Juraj Strossmayer University of Osijek Faculty of Electrical Engineering, Computer Science and Information Technology Osijek. The awards recognize significant personal and professional development and notable contributions to the recipients' respective fields of research over the past five years.

The Croatian Academy of Engineering extends its sincere congratulations to all newly elected and promoted members of the Academy, as well as to the recipients of the 2025 HATZ Awards. Their achievements, professional and scientific contributions, and commitment to the advancement of technical and biotechnical sciences represent lasting value for the Academy, the Croatian scientific community, and society as a whole.

The Academy expresses its sincere gratitude to the University of Zagreb Faculty of Chemical Engineering and Technology for its cooperation and support in organizing the 59th Annual Assembly of HATZ and the 4th Mini Scientific-Professional Conference, as well as for sponsoring the academic gathering that followed.

The Academy also gratefully acknowledges the longstanding support of Centar za vozila Hrvatske d.d. and its financial contribution to the HATZ Awards, which promotes excellence and supports the professional development of young researchers.


59. REDOVITA GODIŠNJA SKUPŠTINA
AKADEMIJE TEHNIČKIH ZNANOSTI HRVATSKE
8. lipnja 2026.


59. REDOVITA GODIŠNJA SKUPŠTINA
AKADEMIJE TEHNIČKIH ZNANOSTI HRVATSKE
8. lipnja 2026.





Engineering Power – *Bulletin of the Croatian Academy of Engineering* Vol. 21(2) 2026 – ISSN 2718-322X (Online)
Publisher: Croatian Academy of Engineering (HATZ), 28 Kačić Street, HR-10000 Zagreb, Republic of Croatia
Editor-in-Chief: Prof. Emeritus Vedran Mornar, Ph.D., President of the Academy
University of Zagreb Faculty of Electrical Engineering and Computing
Editor: Prof. Bruno Zelić, Ph.D., Vice-President of the Academy
University of Zagreb Faculty of Chemical Engineering and Technology
Guest Editor: Prof. Neven Duić, Ph.D., University of Zagreb, Faculty of Mechanical Engineering and Naval Architecture
Activities Editor: Tanja Miškić Rogić
Editorial Board: Prof. Vedran Mornar, Ph.D., Prof. Vladimir Andročec, Ph.D., Prof. Bruno Zelić, Ph.D., Assoc. Prof. Mario Bačić, Ph.D., Prof. Neven Duić, Ph.D.
Editorial Board Address: Croatian Academy of Engineering (HATZ), "Engineering Power" – Bulletin of the Croatian Academy of Engineering, Editorial Board, 28 Kačić Street, HR-10000 Zagreb, Republic of Croatia
E-mail: hatz@hatz.hr
Graphical and Technical Editor: Tiskara Zelina, Ltd., Zelina

The publication of the Engineering Power journal was financially supported by the Ministry of Science, Education and Youth within the project Strengthening publishing activities, cooperation with industry, and the national and international visibility of technical and biotechnical sciences through the programmes and activities of the Croatian Academy of Engineering, pursuant to the Financial Assistance Agreement dated May 20, 2026.